

Mass Determination in SUSY-like Events with Missing Energy

Hsin-Chia Cheng, John F. Gunion, Zhenyu Han, Guido Marandella, and Bob McElrath

Department of Physics, University of California, Davis, CA 95616

E-mail: cheng@physics.ucdavis.edu, jfgucd@physics.ucdavis.edu,
zhenyuan@physics.ucdavis.edu, maran@physics.ucdavis.edu,
mcelrath@physics.ucdavis.edu

ABSTRACT: We describe a kinematic method which is capable of determining the overall mass scale in SUSY-like events at a hadron collider with two missing (dark matter) particles. We focus on the kinematic topology in which a pair of identical particles is produced with each decaying to two leptons and an invisible particle (schematically, $pp \rightarrow YY + jets$ followed by each Y decaying via $Y \rightarrow \ell X \rightarrow \ell\ell' N$ where N is invisible). This topology arises in many SUSY processes such as squark and gluino production and decay, not to mention $t\bar{t}$ di-lepton decays. In the example where the final state leptons are all muons, our errors on the masses of the particles Y , X and N in the decay chain range from 4 GeV for 2000 events after cuts to 13 GeV for 400 events after cuts. Errors for mass differences are much smaller. Our ability to determine masses comes from considering all the kinematic information in the event, including the missing momentum, in conjunction with the quadratic constraints that arise from the Y , X and N mass-shell conditions. Realistic missing momentum and lepton momenta uncertainties are included in the analysis.

Contents

1. Introduction	1
2. Topology of events with missing energy	9
3. Idealized case: Perfect resolution, no combinatorics and no background	11
4. Inclusion of combinatorics, finite resolutions and backgrounds	14
4.1 Finite resolution effects and combinatorics	14
4.2 Backgrounds	23
5. Other processes and mass points	25
5.1 Changing relative mass differences in the chain	25
5.2 Small LSP mass	26
5.3 The SPS1a Point	26
6. Summary and Discussion	30
A. Solution Procedure	33
B. SUSY points	36
B.1 Point I	37
B.2 Point II	38
B.3 Point III	38
B.4 Point IV: SPS1a	38

1. Introduction

As the Large Hadron Collider (LHC) is near completion, we will soon be able to fully explore TeV scale physics. Because of the naturalness problem for the Higgs boson in the context of the Standard Model (SM), it is strongly believed that new physics beyond the SM should appear at or below the TeV scale. There are many possible

candidates for TeV-scale physics beyond the Standard Model, giving rise to various experimental signatures at the LHC. If some new signal is discovered, it is vital to determine the masses and spins of the new particles in order to fully reconstruct the picture of the TeV scale.

Some new physics will be easily identified. For example, if there is a Z' gauge boson accessible at the LHC, one can easily find it by looking for the resonance in the invariant mass distributions of its decay products, *e.g.*, a pair of leptons or jets. In general, if the decays of a new particle involve only visible particles, one can search for it by looking for a bump in various invariant mass combinations of the visible particles and the location of the bump determines the mass of the new particle. On the other hand, if the decays of a new particle always contain one or more invisible particles, the search for the new particle becomes more complicated, as there is no “bump” to look for. In order to detect new physics in such a case, it is necessary to understand the SM backgrounds very well and to then look for excesses above them. Determining the masses of the new particles will also be challenging since we cannot directly measure the energy carried away by the invisible particles. Absent good mass determinations, it will be difficult to reconstruct a full picture of the TeV scale even after new physics is discovered.

A scenario with missing particles is highly motivated for TeV scale physics, independent of the hierarchy problem. If we assume that dark matter is the thermal relic of some weakly interacting massive particles (WIMPs) left from the Big Bang, then the right amount of dark matter in the universe is obtained for a WIMP mass in the 0.1–1 TeV range under the assumption that the electroweak sector mediates the dark matter—SM interaction. The dark matter particle must be electrically neutral and stable on cosmological time scales. If it is produced at a collider, because it is weakly interacting it will escape the detector without being detected, giving missing energy signals. In order for the dark matter particle to be stable, it is likely that there is a new symmetry under which the dark matter particle transforms but all SM particles are neutral, thereby preventing decay of the dark matter particle to SM particles.

LEP has indirectly tested physics beyond the SM. The electroweak precision fit and 4-Fermi contact interaction constraints exclude new particles with masses below $\mathcal{O}(\text{TeV})$ if they are exchanged at tree level, unless their coupling to the SM fermions is suppressed. If there is a symmetry under which the new particles are odd and the SM particles are even, then the new particles can only contribute to the electroweak observables at the loop level. In this case, the bound on the mass of the new particles decreases by about a loop factor, $m \rightarrow m/4\pi$, making the existence of new particles with masses of order a few hundreds of GeV compatible with the data. The message coming from the LEP data is that, if there is any new physics responsible for stabilizing

the electroweak scale, it is very likely to possess such a new symmetry. Thus, the cosmological evidence for dark matter together with the LEP data provide very strong motivation for new particles at or below the TeV scale that are pair produced rather than singly produced.

Almost all the models with dark matter candidates contain additional particles charged under the new symmetry. At a collider, these new particles must also be pair-produced, and if they are heavier than the dark matter particle, they will cascade decay down to it. In many cases, this cascade radiates SM particles in a series of $A \rightarrow Bc$, $1 \rightarrow 2$ decays, in which A and B are new physics particles while c is a SM particle. (In some cases, phase space restrictions force one of the new particles off-shell and $A \rightarrow B^*c \rightarrow Cdc$, $1 \rightarrow 3$ decays are relevant.) Since the final step in the chain will yield a dark matter particle, the typical collider signals for such a scenario will be jets and/or leptons plus missing energy.

Supersymmetry (SUSY) is the most popular candidate for physics beyond the SM and belongs to the above category of models. In SUSY, R -parity conservation implies that the Lightest Supersymmetric Particle (LSP) is stable. In most supersymmetric models the LSP is the lightest neutralino, which is a good dark matter candidate. It appears at the end of every supersymmetric particle decay chain and escapes the detector. All supersymmetric particles are produced in pairs, resulting in at least two missing particles in each event.

Other theories of TeV-scale physics with dark matter candidates have been recently proposed. They have experimental signatures very similar to SUSY: *i.e.* multiple leptons and/or jets plus missing energy. For instance, Universal Extra Dimensions (UEDs) [1, 2], little Higgs theories with T -parity (LHT) [3], and warped extra dimensions with a Z_3 parity [4] belong to this category of models. Being able to reconstruct events with missing energy is thus an important first step to distinguish various scenarios and establish the underlying theory.

Of particular importance will be the determination of the absolute masses of the new particles, including the dark matter particle. First, these masses are needed in order to determine the underlying theory. For example, in the case of SUSY, accurate particle masses are needed to determine the SUSY model parameters, in particular the low-scale soft-SUSY-breaking parameters. These in turn can be evolved to the unification scale (under various assumptions, such as no intermediate-scale matter) to see if any of the proposed GUT-scale model patterns emerge. The accuracy required at the GUT-scale after evolution implies that low-scale masses need to be determined with accuracies of order a few GeV. Second, the mass of the dark matter particle, and the masses of any other particles with which it can coannihilate, need to be determined in order to be able to compute the dark matter relic density in the context of a given

model. Studies [5] suggest that the required accuracy is of order a few GeV. A very important question is then whether or not the LHC can achieve such accuracy or will it be necessary to wait for threshold scan data from the ILC. One goal of this paper will be to find techniques for determining the dark matter particle mass at the LHC with an accuracy that is sufficient for a reasonably precise computation of the relic density.

Most of the SUSY studies carried out thus far have relied on long decay chains of super-particles which produce many jets and/or leptons and large missing energy. Several kinematic variables have been proposed as estimators of the super-particle mass scale, such as \cancel{E}_T , H_T , M_{eff} [6], and M_{T2} [7]. However, these variables measure the mass differences between the super-particles, but not the overall mass scale.

One possible means for determining the overall mass scale is to employ the total cross section. However, the total cross section is very model dependent: it depends on the couplings, the species of the particles being produced, *e.g.*, fermions or bosons, as well as the branching fractions of the decays involved in the process. One needs to have already determined the spins and branching ratios for this to be reliable, a task that is difficult or impossible at the LHC without an ability to determine the four-momenta of all the particles involved in the process. To fully test a potential model, we must first determine the masses of the produced particles using only kinematic information. Once the masses are known, there are many chain decay configurations for which it will be possible to use these masses to determine the four-momenta of all the particles on an event-by-event basis. The four-momenta can then be employed in computing the matrix element squared for different possible spin assignments. In this way, a spin determination may be possible, and then the cross section information can be used to distinguish different models.

In recent years there have been numerous studies of how to measure the super-partner masses just based on kinematic information [6, 8, 9, 10, 11, 12, 13, 14, 15, 16]. These studies rely on long decay chains of super-particles, usually requiring 3 or more visible particles in the decay chain in order to have enough invariant mass combinations of the visible particles. One can then examine the kinematic edges of the distributions of the various invariant mass combinations, and obtain the masses from the relations between the end points of the distributions and the masses. Many of these studies use the decay chain $\tilde{q} \rightarrow \tilde{\chi}_2^0 q \rightarrow \tilde{\ell} \ell q \rightarrow \tilde{\chi}_1^0 \ell \ell q$ (Fig. 1) that occurs for the benchmark point SPS1a [17], for which $m_{\tilde{\chi}_1^0} \sim 97$ GeV, $m_{\tilde{\ell}} \sim 143$ GeV, $m_{\tilde{\chi}_2^0} \sim 180$ GeV, $m_{\tilde{q}} \sim 570$ GeV and $m_{\tilde{g}} \sim 610$ GeV, see Appendix B. The kinematic endpoints of the invariant mass distributions, $m_{\ell\ell}$, $m_{q\ell\ell}$, $m_{q\ell(\text{high})}$, and $m_{q\ell(\text{low})}$ ¹, depend on the masses of the super-

¹High and low represent the largest and the smallest values of $m_{q\ell}$, respectively — these masses are employed since it is not possible to determine the order in which the observed leptons appear in the chain decay.

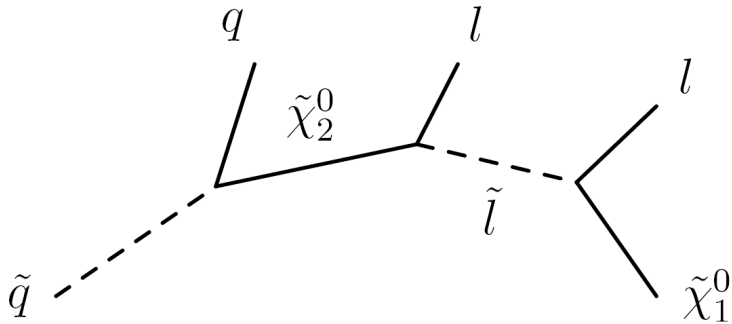


Figure 1: A decay chain in SUSY.

particles in the decay chain through some complicated relations [9, 10, 18]. If the end points of these distributions can be accurately determined from the experimental data, we can invert the relations to obtain the masses of the super-particles.

For the decay chain of Fig. 1 and the specific model points studied, this approach can give a reasonable determination of the masses of the super-particles, but there is room for improvement. In some of the studies, it is only mass differences that are well determined whereas the overall mass scale is rather uncertain. For one of the mass points studied in [10, 18] (labeled α in [10]), a very large number of events is employed and the overall mass scale uncertainty is reduced to two discrete choices, one corresponding to the correct solution (with rms error relative to the central value of order 4 GeV) and the other (somewhat less probable value) shifted by about 10 GeV. For the mass choices labeled β , for which the event rate is lower, there are a number of discrete solutions and each one has fairly large rms error for the absolute mass scale. However, it should be noted that in reducing the solutions to a number of discrete choices, not only were the locations of the kinematic edges employed, but also the shapes of the distributions of the mass combinations were employed. These latter shapes depend upon their choice of model being correct. It is possible that without this information there would have been a significant continuous range of overall possible mass scale.

Another mass determination method is that proposed by Kawagoe, Nojiri, and Polesello [12]. Their method relies on an even longer decay chain, $\tilde{g} \rightarrow \tilde{b}b_2 \rightarrow \tilde{\chi}_2^0 b_1 b_2 \rightarrow \tilde{l} b_1 b_2 \ell_2 \rightarrow \tilde{\chi}_1^0 b_1 b_2 \ell_1 \ell_2$. There are five mass shell conditions and for each event there are the four unknowns due to the unobservable 4-momentum of the $\tilde{\chi}_1^0$. In principle, before introducing combinatorics and experimental resolution, one can then find a discrete set of solutions in the space of the 5 on-shell masses as intersections of the constraints coming from just five events. In practice, combinatorics and resolution complicate the

picture. In their actual analysis, they only fitted the gluino and the sbottom masses *with the assumption that the masses of $\tilde{\chi}_2^0$, $\tilde{\ell}$, and $\tilde{\chi}_1^0$ are already known*. For the standard SPS1a point, they achieved accuracies for $m_{\tilde{g}}$ and $m_{\tilde{b}}$ of order a few GeV, but with central values systematically shifted (upward) by about 4 GeV. In a follow up study [13], Lester discusses a procedure for using all 5 on-shell mass constraints. For a relatively small number of events and without considering the combinatorics associated with the presence of two chains, he finds a 17% error in the determination of $m_{\tilde{\chi}_1^0}$.

In addition to the above studies, a series of contributions concerning mass determination appeared in [11]. These latter studies focused on the SPS1a point and again employed the kinematic edges of the various reconstructable mass distributions in the $\tilde{g} \rightarrow \tilde{b}b_2 \rightarrow \tilde{\chi}_2^0 b_1 b_2 \rightarrow \tilde{\ell} b_1 b_2 \ell_2 \rightarrow \tilde{\chi}_1^0 b_1 b_2 \ell_1 \ell_2$ decay chain to determine the underlying sparticle masses. Experimental resolutions for the jets, leptons and missing energy based on ATLAS detector simulations were employed. The resulting final errors for LHC/ATLAS are quoted in Table 5.1.4 of [11], assuming an integrated luminosity of 300 fb^{-1} and after using both \tilde{e} and $\tilde{\mu}$ intermediate resonances (assuming they are degenerate in mass). We have since verified with several ATLAS members that the quoted errors do indeed correspond to $\pm 1\sigma$ errors [19]. The tabulated errors for $m_{\tilde{\chi}_1^0}$, $m_{\tilde{\ell}}$, $m_{\tilde{\chi}_2^0}$ are all of order 5 GeV, while those for $m_{\tilde{g}}$ and $m_{\tilde{b}}$ are of order 8 GeV.

In all of the studies referenced above, the methods employed required at least three visible particles in the decay chain, and, in the last cases above, four visible particles (two b 's and two ℓ 's). We will study the seemingly much more difficult case in which we make use of only the last two visible particles in each decay chain. (For example, the subcase of Fig. 1 in which only the $\tilde{\chi}_2^0 \rightarrow \ell\ell\tilde{\chi}_1^0$ portion of each decay chain is employed.) In this case, if only the isolated chain-decays are analyzed, the one invariant mass combination that can be computed from the two visible 4-momenta does not contain enough information to determine the three masses ($m_{\tilde{\chi}_2^0}$, $m_{\tilde{\ell}}$ and $m_{\tilde{\chi}_1^0}$) involved in the decay chain. Thus, we pursue an alternative approach which employs both decay chains in the event at once. For the SPS1a point, our method allows a determination of the masses $m_{\tilde{\chi}_2^0}$, $m_{\tilde{\ell}}$ and $m_{\tilde{\chi}_1^0}$ with an accuracy of $\sim \pm 5$ GeV after including both \tilde{e} and $\tilde{\mu}$ intermediate slepton states (again, taken to be degenerate in mass), assuming $L = 300 \text{ fb}^{-1}$ and adopting the ATLAS expectations for the resolutions for lepton momentum and missing momentum measurements. (These resolutions affect the determination of the crucial transverse momentum of the $4\ell + 2\tilde{\chi}_2^0$ system. In particular, by looking at only the leptonic part of the decay chains we can avoid considering individual jet momenta, and therefore we are less sensitive to imprecise measurements for the individual jets.) In short, using only the leptons in the final state, we obtain an accuracy that is very comparable to the $\sim \pm 5$ GeV found in the LHC/ATLAS study referenced above for the same luminosity and very similar detector simulation.

In the above single-chain decay approaches, it is implicitly assumed that appropriate cuts *etc.* have been employed so that both decay chains in each event involve the same decaying resonances, all the way back to the \tilde{g} . In our approach it is unnecessary to know exactly what resonances appear prior to the $\tilde{\chi}_2^0$'s in the two decay chains. Thus, some of the $\tilde{\chi}_2^0$ pair events could come from direct \tilde{q} production and some indirectly from \tilde{g} production followed by $\tilde{g} \rightarrow q\tilde{q}$ decay. We also do not need to tag the b quarks. We only need to measure to determine the transverse momentum of the $\tilde{\chi}_2^0\tilde{\chi}_2^0$ pair using the measured lepton momenta and the measured missing momentum. Nonetheless, we do need to isolate a sample of events dominated by two final $\tilde{\chi}_2^0 \rightarrow \ell\tilde{\ell} \rightarrow \ell\ell\tilde{\chi}_1^0$ decays. (Of course, it is interesting to go beyond this assumption, but we will not do so in this paper.) The key to mass determination using the more limited information we employ is to consider the whole event at once and look not for edges in masses reconstructed from visible momenta but for sharp transitions in the number of events consistent with the assumed topology after an appropriate reconstruction procedure. Further, as noted later, if the events we isolate do not correspond to a $\tilde{\chi}_2^0\tilde{\chi}_2^0$ pair decaying in the manner assumed, then our procedure will yield smooth distributions in the number of reconstructed events, as opposed to the sharp transitions predicted if we have indeed isolated an enriched $\tilde{\chi}_2^0\tilde{\chi}_2^0$ -pair sample with decays as presumed.

Beginning with the general topology illustrated in Fig. 2, we employ the information coming from correlations between the two decay chains in the same event, and the missing momentum measurement. This is evident from some simple constraint counting. Each event satisfying the topology of Fig. 2 has the two invisible 4-momenta of the N and N' . The sum of the transverse momenta of N and N' is, however, constrained to equal the negative of the sum of the transverse momenta of the visible particles, leaving us with 6 unknowns for each event, subject to 6 on-shell mass constraints. Under the assumption that $m_Y = m_{Y'}$, $m_X = m_{X'}$ and $m_N = m_{N'}$, we are left with the three unknown masses, m_Y , m_X and m_N . Every event will be compatible with a certain region in the 3-dimensional $\{m_Y, m_X, m_N\}$ space. Combining several events will shrink this region. We will show that before the inclusion of combinatorics and resolution effects the actual values of the masses lie at the end point of such a region. Mass determination after including combinatoric and resolution effects requires an examination of how the number of events consistent with given mass choices changes as the masses are shifted.

In our approach, we find that it is important to not focus on the individual invariant mass distributions, as this would not utilize all the information contained in the data. Instead, we examine the events from a more global point of view and try to use all the kinematic information contained in the data to determine the masses of the particles involved.² In the case where we have of order 2000 events available after cuts, and after

²We note that the fact that each event defines a region in mass space was also the case for the

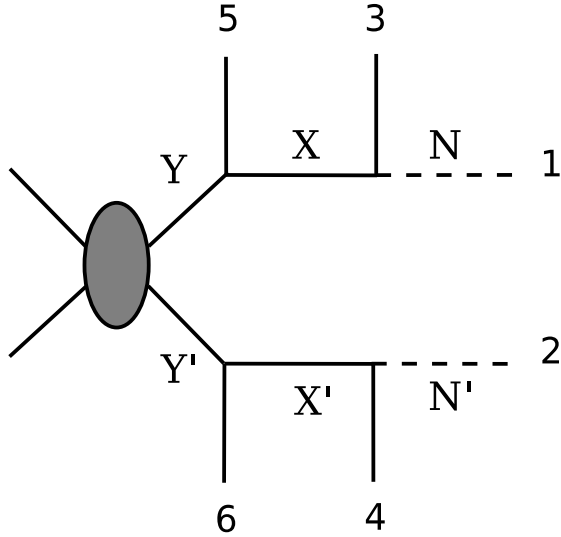


Figure 2: The event topology we consider.

including combinatorics and resolutions for missing momentum and lepton momentum measurements according to ATLAS detector expectations, we achieve rms accuracies on m_Y , m_X and m_N of order 4 GeV, with a small systematic shift that can be easily corrected for. This assumes a case with significant separation between the three masses. This result is fairly stable when backgrounds are included so long as $S/B \gtrsim 2$. This number of events and resulting error apply in particular to the SPS1a point assuming integrated luminosity of $L = 300 \text{ fb}^{-1}$ and use of all $\tilde{\ell} = \tilde{e}$ or $\tilde{\mu}$ channels.

The organization of the paper is as follows. In Sec. 2, we give a detailed exposition regarding solving the topology of Fig. 2. In Sec. 3, we demonstrate how the masses of the Y , X and N particles in Fig. 2 can be very precisely determined after a reasonable number of events (*e.g.* 500) if there are no uncertainties associated with combinatorics or with particle and missing momentum measurement resolutions. In Sec. 4, we develop the very crucial strategies for dealing with the realistic situation where combinatorics, resolutions and backgrounds are included. Sec. 4.1 focuses on the effects of combinatorics and finite resolutions for the lepton and measurement missing momentum measurements. If of order 2000 events are present after cuts, we still find good accuracies for not only mass differences, but also for the absolute mass scale,

$Z \rightarrow Y \rightarrow X \rightarrow N$ one-sided chain situation outlined earlier (except for the mass space being 4-dimensional). An interesting question is whether our more general approach would determine the absolute mass scale in the one-sided case, as opposed to just mass differences. A detailed study is required.

using only the kinematic information contained in the available events. In Sec. 4.2, we discuss the effects of having background events mixed with the signal events. In Sec. 5, we discuss two alternative scenarios: one with very different $m_Y - m_X$ compared to the first point analyzed, and one with $m_N \sim 0$. In Sec. 5.3, we consider in detail the SPS1a mSUGRA point. We summarize and present additional discussion in Sec. 6.

2. Topology of events with missing energy

We study the collider events with topology shown in Fig. 2. A hard hadronic collision produces two identical or mirrored chains. Each decay chain gives two visible particles and one missing particle. It will be convenient to label the 6 final outgoing particles from 1–6, with $N = 1$, $N' = 2$, visible particles 3 and 5 emitted from the Y chain and visible particles 4 and 6 emitted from the Y' chain. There are many processes which have this topology. For example, $t\bar{t}$ production, with t decaying to bW and W decaying leptonically to $\ell\nu$, is exactly described by this topology, so it can be studied with our method, except that we already know that neutrinos are (to a good approximation) massless. There are also many SUSY or other beyond the SM processes which can be described by this topology, *e.g.*, second neutralino pair production $\tilde{\chi}_2^0\tilde{\chi}_2^0$ (through t -channel squark exchange) with $\tilde{\chi}_2^0 \rightarrow \ell\tilde{\ell}$ and then $\tilde{\ell} \rightarrow \ell\tilde{\chi}_1^0$, producing 4 visible charged leptons and 2 missing particles. As already noted, we require that the masses of the corresponding particles in the two chains be the same. They can be the same particle or one can be the anti-particle of the other. Or, they can even be different particles whose masses are believed to be approximately equal (*e.g.*, squarks or sleptons of the first two generations). The visible particles do not need to be stable as long as we can see all their decay products and reconstruct their 4-momenta. The event can involve more particles (such as hadronic ISR/FSR or parent particles such as squarks and gluinos decaying within the gray blob on Fig. 2) as long as none of the additional particles lead to missing momentum. For example, the 4 leptons plus missing energy event from the decays of a pair of second neutralinos can be part of the longer decay chains from squark pair production, as occurs for the SPS1a chain decay.

It is instructive to analyze the unknowns in this topology in a more detailed manner than given in the introduction. In particular, we can make a distinction between *kinematic unknowns* — those in which phase space is differential — and *parametric unknowns* — Lagrangian parameters or otherwise non-kinematic unknowns on which the cross section has some functional dependence. For instance in the Breit-Wigner propagator $[(q^2 - M^2)^2 + M^2\Gamma^2/4]^{-1}$, q is kinematic while M and Γ are parametric. Masses, including those of missing particles, are parametric unknowns (phase space

$d^3p/2E$ is not differential in them). Any function of an event's missing 3-momenta and already-known parameters is a kinematic unknown.

Each event with the topology of Fig. 2 has eight kinematic unknowns: $\vec{p}_N, \vec{p}_{N'}$ and the initial state E and p_z , where we are assuming the parameters m_N and $m_{N'}$ are fixed. Total 4-momentum conservation reduces this to four kinematic unknowns. In the narrow width approximation, the mass combinations constructed from a combination of visible momenta and invisible momenta (which we place in the class of kinematic unknowns), such as $m_{13}^2 \equiv (p_1 + p_3)^2$, are equal to the corresponding parametric unknowns, such as m_X^2 , and we can trade them for their corresponding parameters. Therefore, in the narrow width approximation, a single event is described by a volume in the six dimensional parameter space $\{m_Y, m_{Y'}, m_X, m_{X'}, m_N, m_{N'}\}$.

If the two chains are identical or mirrors of one another and if we use the narrow width approximation, we can impose 3 more relations, $m_Y = m_{Y'}$, $m_X = m_{X'}$ and $m_N = m_{N'}$, which reduces the independent unknown parameters to three. As a result, if we know the three masses m_Y , m_X , and m_N then (up to discrete ambiguities associated with multiple solutions to a quartic equation) we can solve for all the unknown momenta, using the measured visible momenta, and vice versa. The procedure is described in more detail in Appendix A.

If the masses are not known, we must assume values for the three masses m_Y , m_X , and m_N . Given a fixed $\mathcal{M} = \{m_Y, m_X, m_N\}$ choice, for each event we obtain a quartic equation (for the energy of one of the invisible particles) with coefficients depending on the assumed masses, \mathcal{M} , and visible momenta. It can have 0 to 4 real solutions for the invisible energy, depending on the coefficients, and each solution fully determines associated 4-momenta for both invisible particles.

Any solution with real and physically acceptable invisible 4-momenta corresponds to a choice for m_Y , m_X , and m_N that is consistent with that particular event. The points in $\mathcal{M} = \{m_Y, m_X, m_N\}$ parameter space that yield real solutions are not discrete; instead, each event defines a region in the three-dimensional mass space corresponding to a volume of real solutions. The region in the mass space consistent with all events, the 'allowed' region, will shrink as we consider more and more events. However, even for many events the allowed region remains three-dimensional and does not shrink to a point. We need to find techniques that allow us to identify the correct mass point given a volume in mass space consistent with a set of events.

3. Idealized case: Perfect resolution, no combinatorics and no background

In order to understand how the mass information is contained in the kinematics, we start with the ideal case in which all visible momenta are assumed to be measured exactly and we associate each lepton with the correct chain and position in the chain (*i.e.*, we neglect resolution effects and combinatorics). For illustration, we have generated a sample of 500 events of $\tilde{q}_L\tilde{q}_L$ production, with each \tilde{q}_L decaying according to Fig. 1, with $Y = Y' = \tilde{\chi}_2^0$, $X = X' = \tilde{\mu}_R$, $N = N' = \tilde{\chi}_1^0$, and 3, 4, 5, 6 all being μ 's of various signs. We generated our events using SHERPA [20] versions 1.0.8 and 1.0.9 and PYTHIA [21]. We generated the SUSY spectrum for the mass points considered using SPheno 2.2.3 [22]. Details regarding the spectrum, cross sections and branching ratios for this point (Point I) are given in Appendix B. For the moment, we only need to note the resulting masses:

$$m_Y = 246.6 \text{ GeV}, \quad m_X = 128.4 \text{ GeV}, \quad m_N = 85.3 \text{ GeV}. \quad (3.1)$$

We stress however that our techniques are not specific to SUSY; we have just used the available tools for supersymmetric models. Thus, event rates employed are not necessarily those predicted in the context of some particular SUSY model. Here, we simply use a 500 event sample for illustration of the basic ideas.

For simplicity, we have required all four leptons to be muons. We assume that the momenta of the 4 muons and the sum of the transverse momenta of the two neutralinos are known exactly. The only cuts we have applied on this sample are acceptance cuts for the muons: $p_T > 6 \text{ GeV}$ and $|\eta| < 2.5$. We do not consider the mass of the squark, therefore information from the quarks is irrelevant except that the presence of the quark jets typically boosts the system (Fig. 2) away from the z axis, an effect automatically included in our analysis. In the following, we denote a set of masses as $\mathcal{M} = \{m_Y, m_X, m_N\}$ and the correct set as \mathcal{M}_A .

Each event defines a mass region in \mathcal{M} space that yields real solutions for \vec{p}_N and $\vec{p}_{N'}$ (for which we often employ the shorter phrase ‘real solutions’ or simply ‘solutions’). This region can be determined by scanning through the mass space. We then examine the intersection of the mass regions from multiple events. This region must contain the correct masses, \mathcal{M}_A . The allowed mass region keeps shrinking when more and more events are included. One might hope to reach a small region near \mathcal{M}_A as long as enough events are included. However, this is not the case, as exemplified in Fig. 3. There, the 3-dimensional allowed region in \mathcal{M} -space is shown together with its projections on 2-dimensional planes. When producing Fig. 3, we discretize the mass space to 1 GeV grids in all three directions. As already noted, we have used the correct assignments

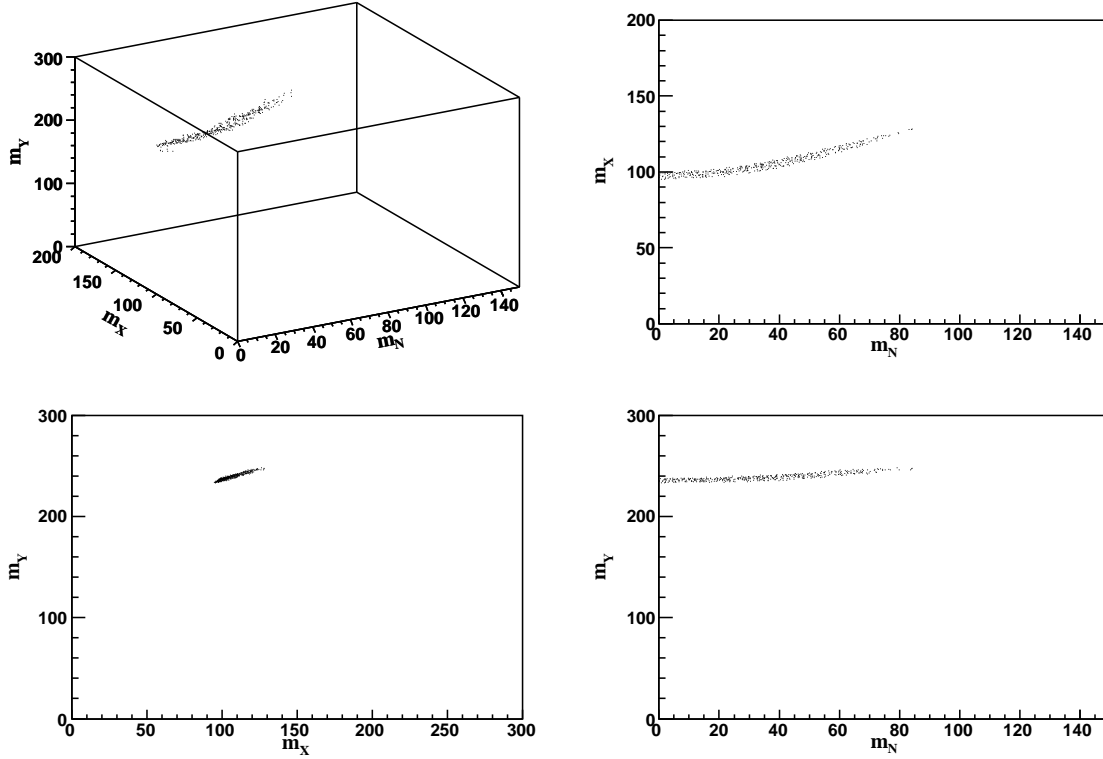


Figure 3: Mass region (in GeV) that can solve all events for the input masses $\{m_Y, m_X, m_N\} = \{246.6, 128.4, 85.3\}$ GeV using 500 events.

for the locations of the muons in the decay chains. Wrong assignments will add more complication; this will be discussed in Sec. 4. With correct assignments, and because of our narrow-width and no-smearing assumptions, the correct masses \mathcal{M}_A will result in at least one real \vec{p}_N and $\vec{p}_{N'}$ solution for all events and is included in the allowed region. In all three 2-dimensional projections, the entire allowed region is a strip with m_Y and m_X close to the correct values, but m_N left undetermined except for an upper bound. A lower bound is sometimes present and can be caused by the presence of events in which the system (Fig. 2) has a large amount of transverse momentum. The upper bound for m_N generally materializes using fewer events than does the lower bound. By examining the figures one can see that the upper bound for m_N is actually close to the correct m_N ; more generally, \mathcal{M}_A is located near the tip of the cigar shape of acceptable choices in \mathcal{M} -space.

An intuitive understanding of why it is that the correct mass set \mathcal{M}_A is located at an end point can be garnered from Fig. 4. Any point in the mass space on the left-hand

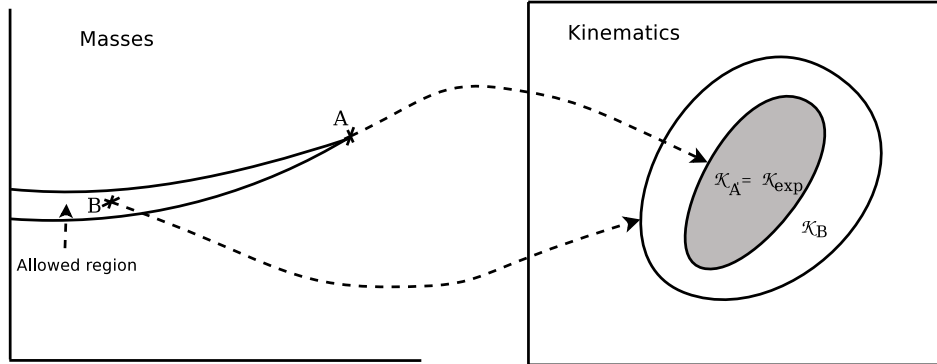


Figure 4: Map between mass space and kinematic space. The nominal masses, point A , produces a kinematic region that coincides with the experimental region: $\mathcal{K}_A = \mathcal{K}_{exp}$. A point B inside the allowed mass region produces a larger kinematic region: $\mathcal{K}_B \supset \mathcal{K}_{exp}$.

side of the figure is mapped into a *region* of the kinematic space on the right-hand side. By ‘kinematic space’ we mean the set of observed 3-momenta of the visible particles, 3, 4, 5, and 6. Thus, the kinematic space has much higher dimensionality than the mass space — the on-shell Y, X, N masses can be held fixed while changing the angles, magnitudes and so forth of the visible particles. Consequently, each point in mass space defines a volume in kinematic space. In analyzing data, the inverse mapping is to be envisioned. Each point in the kinematic space corresponds to a specific momentum configuration of the visible particles, *i.e.* an event. A collection of many events will define a region in the kinematic space. In particular, the correct set of masses, point A in Fig. 4, produces a kinematic region \mathcal{K}_A that coincides with the experimental one, $\mathcal{K}_A = \mathcal{K}_{exp}$, as long as the number of experimental events is large enough so that all the allowed region is populated. Any shift away from A will generally not allow one or more kinematical observables associated with the visible particles to occupy a region close to the boundary of \mathcal{K}_{exp} ; *i.e.* such a shift will generally exclude a region of the actually observed kinematical space.

A mass point other than \mathcal{M}_A produces a region different from \mathcal{K}_{exp} . If it does not cover the entire \mathcal{K}_{exp} , this means that some events will not have yielded real \vec{p}_N and $\vec{p}_{N'}$ solutions and, therefore, the mass point does not appear in the final allowed mass region. On the other hand, there can be mass points which produce larger kinematic regions encompassing the entire \mathcal{K}_{exp} region. These mass points yield real solutions for all events and hence belong to the final allowed region. This kind of point is exemplified by point B in Fig. 4. If we shift such a point in the mass space by a small amount, $\mathcal{M}_B \rightarrow \mathcal{M}' = \mathcal{M}_B + \delta\mathcal{M}$, the resulting kinematic region still covers \mathcal{K}_{exp} . In this case,

\mathcal{M}' still yields real solutions for all events. Thus, point B , which produces a region larger than \mathcal{K}_{exp} , has the freedom to move in many directions because it lives inside the allowed region rather than on its boundary. On the other hand, the correct mass point A , which produces exactly \mathcal{K}_{exp} , has the least freedom to move. In short, locating the correct mass point \mathcal{M}_A can be viewed as a kind of generalization of the ‘edge’ method which employs sharp edges in certain invariant mass combinations constructed from the visible momenta. Our method matches the whole boundary of the allowed region in the high-dimensional kinematic space of the visible momenta.

Of course, using the “tip” of the allowed mass region is not applicable in the realistic case where experimental resolutions and combinatorics are included, not to mention the possible presence of background events. In particular, some of the events generated after including these effects will be inconsistent (*i.e.* not yield real solutions for p_N and $p_{N'}$) with the correct mass set \mathcal{M}_A and so this point will not be contained in the \mathcal{M} volume obtained if all events are considered. We must find more sophisticated methods to identify the correct mass point. Nevertheless, understanding the idealized case provides useful guidance for understanding how to deal with the more complicated realistic situations.

4. Inclusion of combinatorics, finite resolutions and backgrounds

In this section we discuss the more realistic case with finite resolutions, combinatorics and backgrounds. We first discuss the effects from finite resolutions and combinatorics and later we will include the backgrounds. For the moment, we continue to employ the spectrum associated with the SUSY Point I, as specified in Appendix B, with $\{m_Y, m_X, m_N\} = \{246.6, 128.4, 85.3\}$ GeV.

4.1 Finite resolution effects and combinatorics

Experimental effects related to smearing and combinatorics will deform or even kill the allowed mass region. In particular, since the correct mass point is located at the endpoint, it is most vulnerable to any mismeasurement. This can be seen in Fig. 5, which corresponds to 500 events for the same mass point as Fig. 3. The difference is that we have: i) added smearing; ii) considered all possible combinatoric assignments for the location of the muons in the two decay chains; and iii) included the finite widths of the Y and X intermediate resonances. We smear muon momenta and missing p_T using the low-luminosity options of the ATLAS fast simulation package `ATLFAST` as described in Secs. 2.4 and 2.7 of [23]. Very roughly, this corresponds to approximately Gaussian smearing of muon momentum with width $\sim 3\%/p_T$ and of each component of missing momentum p_T^{miss} with width ~ 5.8 GeV. We note that we are not directly

sensitive to the resolution associated with individual jet momentum measurements; uncertainties in the determination of individual jet momenta are, of course, reflected in the uncertainty of the determination of p_T^{miss} as we shall shortly review. Our approach is only sensitive to p_T^{miss} uncertainties because we do not look at the jets associated with the chain decays prior to arriving at the $\tilde{\chi}_2^0\tilde{\chi}_2^0$ pair. We only need the net transverse momentum of the $\tilde{\chi}_2^0\tilde{\chi}_2^0$ pair as a whole, and we determine this in our procedure as $\sum_\ell p_T^\ell + p_T^{\text{miss}}$. Thus, in our analysis the errors from smearing derive entirely from the uncertainties in the lepton and missing momentum measurements. The fact that we don't need to look at individual jets is, we believe, an important advantage of our approach to determining the $\tilde{\chi}_2^0$, $\tilde{\ell}$ and $\tilde{\chi}_1^0$ masses. Of course, once these masses have been determined, the edge techniques, which fix mass differences very accurately, can be used to extract the \tilde{g} and \tilde{q} masses.

We summarize the missing energy procedure as described in Sec. 2.7 of [23] in a bit more detail. The missing transverse energy E_T^{miss} is calculated by summing the transverse momenta of identified isolated photons, electrons and muons, of jets, b -jets and c -jets, of clusters not accepted as jets and of non-isolated muons not added to any jet cluster. Finally, the transverse energies deposited in cells not used for cluster reconstruction are also included in the total sum. Transverse energies deposited in unused cells are smeared with the same energy resolution function as for jets. From the calculation of the total sum E_T^{obs} the missing transverse energy is obtained, $E_T^{\text{miss}} = E_T^{\text{obs}}$ as well as the missing transverse momentum components, $p_x^{\text{miss}} = -p_x^{\text{obs}}$ and $p_y^{\text{miss}} = -p_y^{\text{obs}}$.

For combinatorics, we assume no charge misidentification. Then, there are 8 independent possible combinatoric locations for one event, which can be reduced if one muon pair is replaced by an electron pair. If any one of these 8 possibilities yields a real solution (after including smearing/resolution as described above), we include the \mathcal{M} point in our accepted mass region.

As regards the resonance widths, these have been computed within the context of the models we have considered, as detailed in Appendix B. In our Monte Carlo, the mass of a given $\tilde{\chi}_2^0$ or $\tilde{\ell}$ resonance is generated according to a Breit Wigner form using the computed width. Although there will be some model dependence of the widths in that they might differ between the SUSY models employed as compared to a little-Higgs model, the widths for these weakly interacting particles are all much smaller than detector resolutions in both models (*e.g.* of order a few hundred MeV in the SUSY models). This is again an advantage of our approach since we never need to know where on the Breit-Wigner mass distribution of the \tilde{g} and \tilde{q} resonances a given event occurs. We only need the net transverse momentum of the $\tilde{\chi}_2^0\tilde{\chi}_2^0$ system as determined from $\sum_\ell p_T^\ell + p_T^{\text{miss}}$. Also, for the moment we will focus on events with four μ 's in the final

state and so both sleptons in the two decay chains will be $\tilde{\mu}$'s. When we come to the SPS1a mSUGRA point, we will discuss combining results for the $\tilde{\mu}\tilde{\mu}$, $\tilde{e}\tilde{e}$ and $\tilde{\mu}\tilde{e}$ decay channels. Even in this case, we analyze final states with definite lepton composition (4μ , $4e$ or $2e2\mu$) separately and do not need to worry about whether the $\tilde{\mu}$ is closely degenerate with the \tilde{e} (although it in fact is). If there is significant non-degeneracy, that would emerge from our analysis. However, to get final errors on the $\tilde{\ell}$ mass as low as ~ 5 GeV, degeneracy of the $\tilde{\mu}$ and \tilde{e} must be assumed (and of course is predicted in the model). If in some other model, the $\tilde{\mu}$ and \tilde{e} are not degenerate, then errors on these individual masses will be of order $\sim 10 - 12$ GeV, but errors on $m_{\tilde{\chi}_1^0}$ and $m_{\tilde{\chi}_2^0}$ will only be slightly larger than the ~ 5 GeV level since the different channel analyses can be combined for their determination.

The effects of both wrong combinations and smearing are manifest in Fig. 5: wrong combinations increase the chance that a given event can be ‘solved’³ and therefore broaden the allowed region for low m_N . On the other hand, the allowed region has shrunk in the m_N direction with the new upper bound corresponding to a much smaller value. This can also be understood by using Fig. 4: some events near the boundary of \mathcal{K}_A can be resolution-smearred to a location outside of \mathcal{K}_A , which renders \mathcal{K}_{exp} larger than \mathcal{K}_A . Thus the correct mass point A is removed from the allowed mass region. For point B which corresponds to a larger kinematic region, if the fluctuation is small enough, \mathcal{K}_{exp} is still within \mathcal{K}_B and therefore does not disappear. Of course, if the smearing is large, the entire allowed region can be eliminated. The effect from background events, as considered in the next subsection, will be similar. Since background events are produced by some completely different processes there is no reason to expect that multiple background events can be solved by the assumed topology with a given choice of \mathcal{M} . Thus, background events tend to reduce the allowed region.

From the above observation, one concludes that allowed mass region in general does not exist and, even if it exists, we can not read directly from it the correct masses. Some other strategy must be employed. An obvious choice is to examine the number of solvable events for various given masses. We can not simply maximize the number of solvable events and take the corresponding masses as our estimate—such a procedure would still favor low m_N values. Instead, we choose to look for the mass location where the number of solvable events changes drastically. This kind of location is most easily illustrated in one dimension. For example, in Fig. 6 a, we fix m_Y and m_X to the correct (input) values, and count the number of solvable events as a function of m_N . (In this figure and the following discussion, we use bin size of 0.1 GeV). A sudden drop around the correct m_N is obvious. Similarly, in Figs. 6 b and 6 c we have fixed m_Y and m_N

³We define a ‘solved’ event to be an event such that the given $\{m_Y, m_X, m_N\}$ choices yield at least one solution to the final quartic equation that leads to physically allowed values for \vec{p}_N and $\vec{p}_{N'}$.

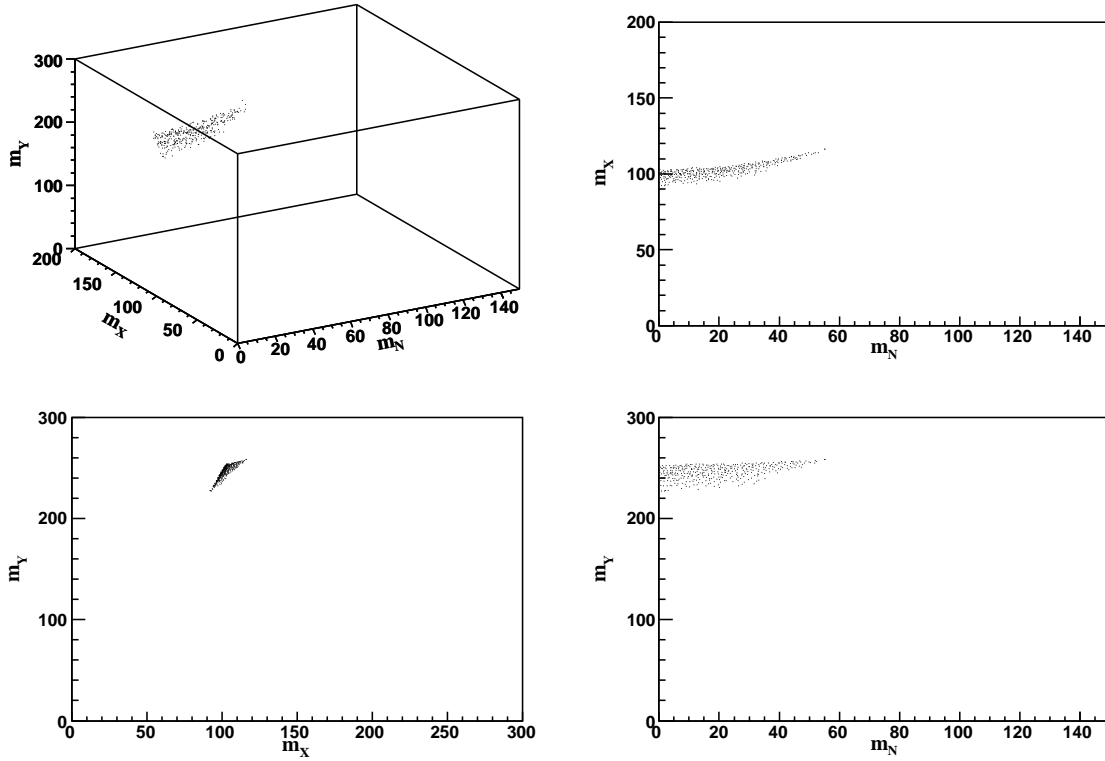


Figure 5: The allowed mass region (in GeV) with smearing and wrong combinatorics.

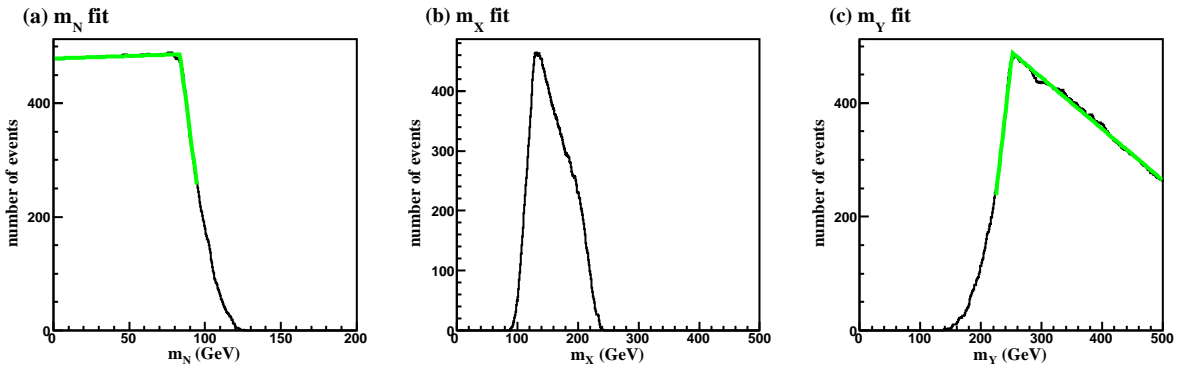


Figure 6: One-dimensional fits by fixing the other two masses at the correct values.

(m_X and m_N) and also see clear “turning points” near the correct m_X (m_Y) mass. To pin down where the turning points are located, we fit Figs. 6 a and 6 c to two straight line segments and take the intersection point as the turning point.

We can not fix *a priori* two of the masses to the correct values since they are unknown. On the other hand, to search for the sharpest turning point directly in the 3-dimensional space is numerically non-trivial. This observation motivates us to obtain the masses from a series of one-dimensional fits. We start from some random set of masses and carry out a recursive series of one-dimensional fits to the number of solved events as a function of m_N , m_X or m_Y holding $\{m_Y, m_X\}$, $\{m_Y, m_N\}$, or $\{m_X, m_N\}$ fixed, respectively. Each such one dimensional fit gives us a sharp turning point that is used to set an updated value for m_N , m_X or m_Y , respectively. We use this new value in performing a fit for the next mass in the sequence in the next step. One might hope that this procedure will converge to the correct mass values, but in practice, even though the procedure passes through the correct mass point, the fitted masses keep increasing and the recursion does not stabilize at the correct mass point. However, as we will see, there is a simple way to get the masses out of the fits.

Having discussed the main ingredients of the method, we present a specific procedure for obtaining the masses. The procedure is applied to a data sample corresponding to 90 fb^{-1} at the LHC, using the event rates and branching ratios obtained for the SUSY Point I as detailed in Appendix B, which, in particular, gives the same masses as those employed in Sec. 3: $\{m_Y, m_X, m_N\} = \{246.6, 128.4, 85.3\} \text{ GeV}$. Taking into consideration the decay branching ratios, the number of events is roughly 2900. In order to mimic reality as much as possible, experimental resolutions and wrong combinatorics are included. To reduce the SM background, we require that all muons are isolated and pass the kinematic cuts:

$$|\eta|_\mu < 2.5, \quad p_{T\mu} > 10 \text{ GeV}, \quad \cancel{p}_T > 50 \text{ GeV}. \quad (4.1)$$

With these cuts, the four-muon SM background is negligible. The number of signal events is reduced from 2900 to about 1900.

The procedure comprises the following steps:

1. Randomly select masses $m_Y > m_X > m_N$ that are below the correct masses (for example, the current experimental limits).
2. Plot the number of solved events, N_{evt} , as a function of one of the 3 masses in the recursive order m_N, m_X, m_Y with the other two masses fixed. In the case of m_Y and m_N , we fit N_{evt} for the plot with two straight lines and adopt the mass value at the intersection point as the updated mass. In the case of m_X , the updated mass is taken to be the mass at the peak of the N_{evt} plot.

A few intermediate one-dimensional fits are shown in Fig. 7.

3. Each time after a fit to m_N , record the number of events at the intersection (sometimes called the turning point) of the two straight lines, as exemplified in Fig. 6 a. This event number at the turning point will in general be non-integer.
4. Repeat steps 2 and 3. The number of events recorded in step 3 will in general increase at the beginning and then decrease after some steps, as seen in Fig. 8. Halt the recursive procedure when the number of (fitted) events has sufficiently passed the maximum position.
5. Fit Fig. 8 to a (quartic) polynomial and take the position where the polynomial is maximum as the estimated m_N .
6. Keep m_N fixed at the value in step 5 and do a few one-dimensional fits for m_Y and m_X until they are stabilized. Take the final values as the estimates for m_Y and m_X .

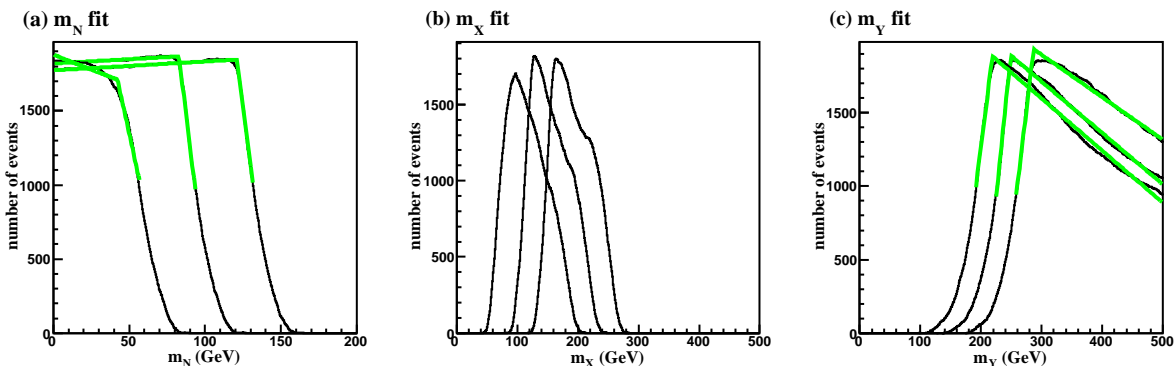


Figure 7: A few steps showing the migration of the one dimensional fits. The middle curve in each plot corresponds to masses close to the correct values.

A deeper understanding of our procedure can be gained by examining the graphical representation of the steps taken in the (m_Y, m_N) plane shown in Fig. 9. There, we display contours of the number of (fitted) events after maximizing over possible m_X choices. The contours are plotted at intervals of 75 events, beginning with a maximum value of 1975 events. As we go from 1975 to 1900 and then to 1825 events, we see that the separation between the contours decreases sharply and that there is a ‘cliff’ of falloff in the number of solved events beyond about 1825 events. It is the location where this cliff is steepest that is close to the input masses, which are indicated by the (red) star. The mass obtained by our recursive fitting procedure is indicated by the (blue) cross. It is quite close to the actual steepest descent location. It is possible

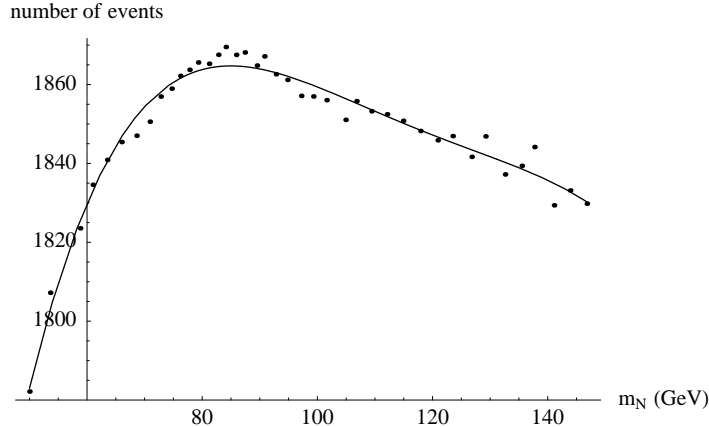


Figure 8: The final plot for determining m_N . The position of the maximum of the fitted polynomial is taken to be the estimation of m_N .

that use of the contour plot by visually picking the point of steepest descent might also yield an accurate mass determination comparable to or possibly even superior to that obtained (and specified in detail below) using the recursive fitting procedure. Roughly, the steepest descent point corresponds to the point where the magnitude of $\vec{\nabla}^2$ in mass space is maximized. Unfortunately, even after some smoothing, the second derivative is quite ‘noisy’ and therefore not particularly useful in a local sense. The one-dimensional fits give us a quick and intuitive way to find this maximum, and the associated recursive procedure has the advantage of being insensitive to statistical fluctuations in the number of events at a single point. Of course, if one has the computer power, probably the most accurate procedure would be to directly fit the 3-d N_{evt} vs. $\{m_Y, m_X, m_N\}$ histogram. Fig. 9 is constructed from a 1-d projection of the 3-d space, and has therefore lost some information.

Following the recursive fitting procedure, the final values for the masses are determined to be $\{252.2, 130.4, 85.0\}$ GeV, which are all within a few GeV of the actual input values, $\{246.6, 128.4, 85.3\}$ GeV. The procedure is empirical in the sense that many of the steps could be modified and improved. In particular, above we adopted the criterion that the correct masses maximize the number of events at the turning points in the m_N fits, which is justified by Fig. 7 a. Instead, we might opt to maximize the number of events in the m_X fits shown in Fig. 7 b. One could also change the order of fits in step 2 and change the fit function from straight lines to more complicated functions, *etc.* We have tried several different strategies and they yield similar results. Finally, one could simulate the signal for a mass point and directly generate Fig. 7, changing the masses until we get the best possible fit to the data; but, this is very

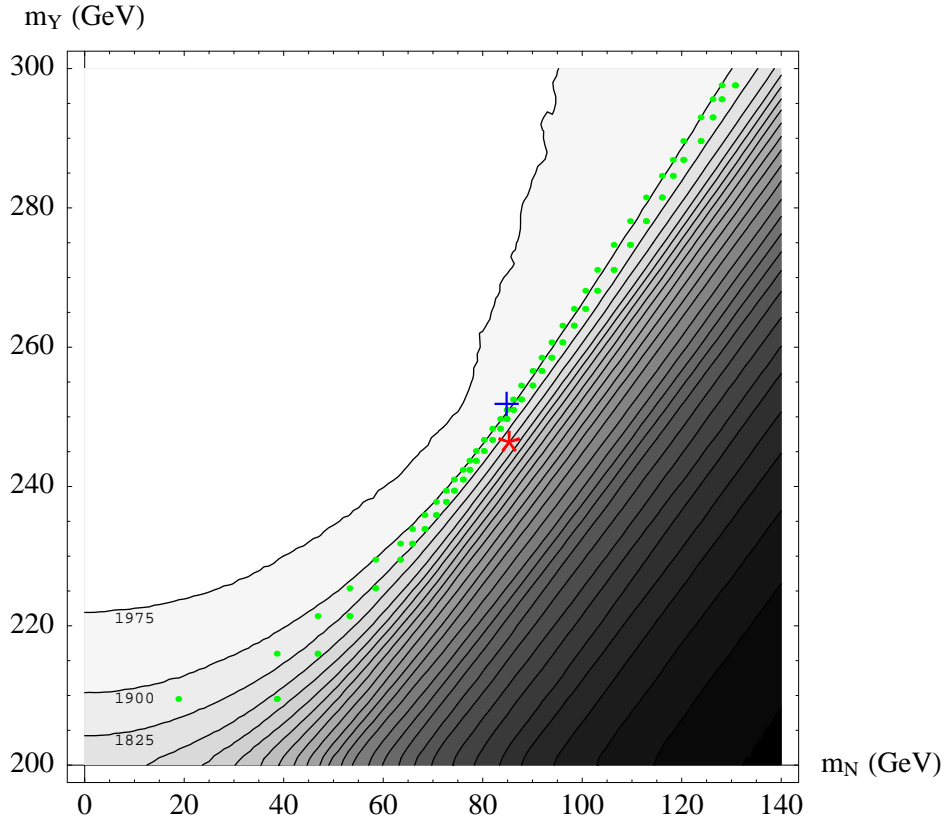


Figure 9: Contours for the number of solved events in the $m_N \sim m_Y$ plane with 2000 events. The number of events is the maximum value obtained after varying m_X . Contours are plotted at intervals of 75 events, beginning with a maximum value of 1975. The red star is the position for the correct masses and the blue cross is the position of the fitted masses. The green dots correspond to a set of one-dimensional fits.

computationally intensive.

The recursive procedure does not provide an easy way to evaluate the errors in the mass determination. For this purpose, we generate 10 different data samples and apply the procedure to each sample. As above, each sample corresponds to 1900 experimental data points after cuts. Then, we estimate the errors of our method by examining the statistical variations of the 10 samples. This yields central masses and rms errors of

$$m_Y = 252.2 \pm 4.3 \text{ GeV}, \quad m_X = 130.4 \pm 4.3 \text{ GeV}, \quad m_N = 86.2 \pm 4.3 \text{ GeV}. \quad (4.2)$$

The statistical variations for the mass differences are much smaller:

$$m_Y - m_X = 119.8 \pm 1.0 \text{ GeV}, \quad m_X - m_N = 46.4 \pm 0.7 \text{ GeV}. \quad (4.3)$$

Compared with the correct values, $\mathcal{M}_A = \{246.6, 128.4, 85.3\}$ GeV, we observe small biases in the mass determination, especially for the mass differences, which means that our method has some “systematic errors”. (The biases will, of course, depend upon the particular functions employed for the one dimensional fits — our choice of using straight lines is just the simplest.) One technique for determining the biases is to perform our analysis using Monte Carlo data. In particular, one could examine the plots of number of ‘solved’ events vs. test mass as obtained from the data vs. those obtained from a Monte Carlo in which definite input masses (which are distinct from the test masses employed during our recursive procedure) are kept fixed. One would then search for those input masses for which the distributions of the solved event numbers from the Monte Carlo match those from the data. Knowing the underlying Monte Carlo masses as compared to the extracted masses would allow us to subtract the differences, thereby removing the biases. This procedure would not appreciably change the errors quoted above. We believe that the biases are mainly a function of the underlying masses and broad kinematic event features. However, there may be some weak dependence of the biases on the actual model being employed. Within the context of a given, *e.g.* SUSY, model, the bias can be quite accurately determined.

In the above error estimation, we have neglected the uncertainties coming from varying the choice of the starting point in mass space used to initiate the recursive sequence of fits. This may introduce an error for the absolute mass scale of order the step size around the correct masses. For the masses chosen, it is about 1 GeV and much smaller than the uncertainties from varying data samples.

The reader may be surprised at the small size of the errors quoted above given that the error in the measurement of the missing momentum of any one event is typically of order 5 GeV or larger. The explanation is similar to that associated with understanding the small errors for the edge locations in the edge approach. In the edge approach, the location of the edge for some mass variable m_{vis} is obtained by fitting data obtained at several m_{vis} values. Each such data point has many contributing events and the average value will obviously have much smaller error than the value for any one contributing event. The fit to the edge will further reduce sensitivity to individual events. In our approach, the edge in the distribution of N_{evt} as a function of one of the trial masses (m_N , m_X or m_Y) will similarly be an average over many events and the uncertainty of the location of this edge will be much smaller than the uncertainties in the measurements of the lepton momenta and missing momentum of any one event.

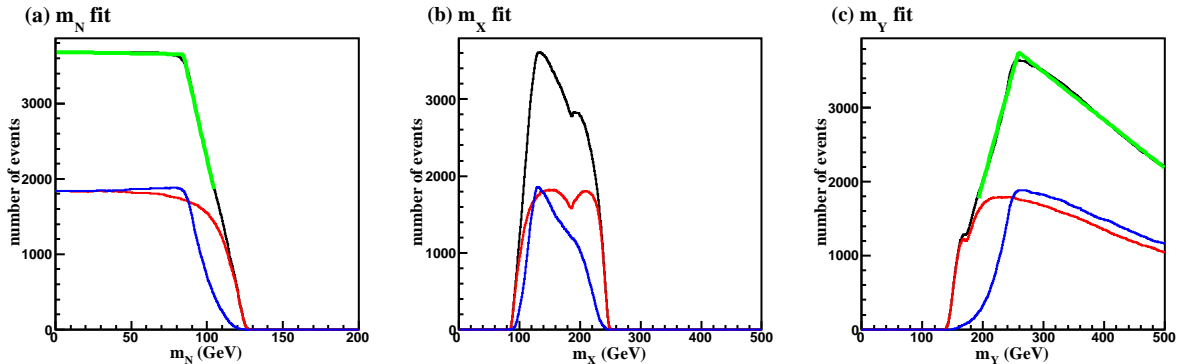


Figure 10: Fits with 1900 signal events (after cuts) and an equal number of background events. Separate numbers of signal (blue) and background (red) events are also shown.

4.2 Backgrounds

For the point we have chosen with a 4 muon + missing energy final state, the background is negligible. We examined backgrounds arising from ZZZ , ZWW , $t\bar{t}$, $t\bar{t}Z$, $t\bar{t}b\bar{b}$, and $b\bar{b}b\bar{b}$. Muons from bottom and charm decays are never very hard nor isolated, and can be easily separated from the signal with basic isolation criteria. Tri-boson production simply has tiny cross sections, especially after requiring all-leptonic decays.

Thus, we must ‘artificially’ introduce background in order to see what its effect might be on our procedures. For this purpose, we generate $t\bar{t}$ events, where the W ’s decay to muons. We require that the b quarks decay to muons, *but do not require them to be isolated*. In many ways, this is a near-worst case background since it has a similar topology aside from the final $b \rightarrow \mu + \dots$ decays. However, the missing neutrinos imply that the missing momentum may be significantly different. As noted, this is not a realistic background as it could be removed by simple isolation cuts on the muons.

Adding a number of background events equal to the number of signal events, *i.e.* 1900 events after cuts, we repeat the one-dimensional fits. A typical cycle around the correct masses is shown in Fig. 10. For comparison the numbers of solvable signal events and background events are also shown separately. The effect of background events is clear: the curve for solvable background events is much smoother around the turning point, and therefore smears but does not destroy the turning point. Although we are considering one specific background process, this effect should be generic, unless the backgrounds happen to have non-trivial features around the turning points. Nevertheless, due to the fact that there are 8 possible combinatoric muon locations, the chance that a background event gets solutions is quite large and they do affect the errors and biases of the mass determination. This can be seen in Fig. 11, in which we have used

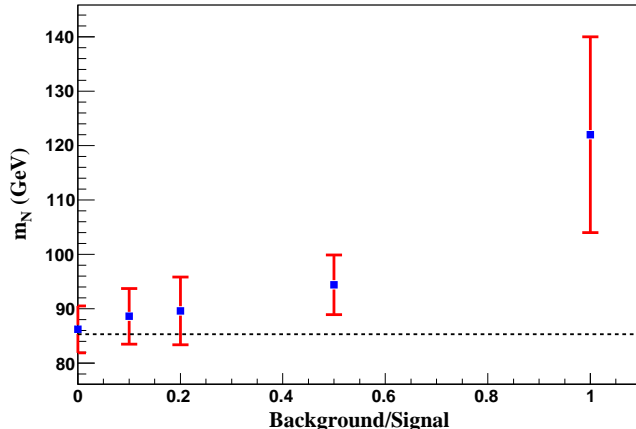


Figure 11: m_N determination with different background-signal ratio. The dashed horizontal line corresponds to the correct m_N .

the same 10 sets of signal events as in the previous subsection, but varied the number of background events according to the ratio $B(\text{ackground})/S(\text{ignal}) = 0, 0.1, 0.2, 0.5, 1$. We observe increases in both the biases and variations about the central values. For $B/S \geq 1$, the maximum in the m_N determination is obscured or even lost and we start to get random results. For $B/S \lesssim 0.2$, we are close to the $B = 0$ results.

It is important to emphasize that the above analysis is pessimistic in that it assumes that we do not understand the nature/source of the background events. One procedure that could significantly improve on uncertainties associated with the background would be to Monte Carlo the background or use extrapolations of measured backgrounds (*e.g.* those as measured before the cuts that make the signal a dominant as compared to a small component of the observed events) and then apply our recursive procedure to the known background and at each stage subtract off the background contribution to a given plot of the number of events vs. m_N , m_Y or m_X . After such subtraction, the recursive procedure will yield essentially identical results to that obtained in the absence of background unless the background itself is not smooth in the vicinity of the ‘turning’ points.

The importance of finding cuts that both select a given topology and minimize background is clear. If it should happen that the we assume the wrong topology for the events retained, then our analysis itself is likely to make this clear. Indeed, events with the “wrong” topology would almost certainly yield a smooth distribution in plots of retained event number vs. any one of the masses of the resonances envisioned as part of the wrong topology. It is only when the correct topology is employed that sharp

steps will be apparent in all the event number vs. resonance mass plots.

Another important situation to consider is that in which it is impossible to find a set of cuts that isolates just one type of decay topology, so that there are several signal processes contributing after a given set of cuts. However, it is quite easy to find situations where there are different signal processes yielding very similar final decay topologies, all of which would be passing through our analysis. One must then look for additional tricks in order to isolate the events of interest. In some cases, this is possible on a statistical, but not event-by-event basis. The SPS1a SUSY point provides an interesting example that we will consider shortly.

5. Other processes and mass points

Our method is generic for the topology in Fig. 2, and in particular is not restricted to the SUSY process we have considered so far. The statistical variations and biases probably do depend to some extent on the process. For example, if the visible particles 5 (6) and 3 (4) are of different species, the number of wrong combinatorics will be reduced and we would expect a better determination of the masses. On the other hand, if one or more of the visible particles are jets, the experimental resolution and therefore the statistical error will be worse than in the 4-lepton case.

5.1 Changing relative mass differences in the chain

The errors in the mass determination also depend on the mass point, especially the two mass differences, $\Delta m_{YX} = m_Y - m_X$ and $\Delta m_{XN} = m_X - m_N$. In Fig. 12, a set of one-dimensional fits are shown for mass point $\mathcal{M} = \{180.8, 147.1, 85.2\}$ GeV (which we label as Point II). We will assume 2000 events after cuts, very similar to the 1900 events remaining after cuts for Point I. Point II differs from Point I in that for Point II $\Delta m_{YX} < \Delta m_{XN}$, while for Point I $\Delta m_{YX} > \Delta m_{XN}$. The double peak structure in the Point II m_X fit (Fig. 12 b) is evident. The curve to the right of the turning point in Fig. 12 c is also “bumpy” compared with Fig. 6 c. These features are induced by wrong combinatorics. In the process we consider, all visible particles are muons, so they could be misidentified as one another and still yield solutions. Roughly speaking, Δm_{YX} and Δm_{XN} determine the momentum of the particles 5 (6) and 3 (4) in Fig. 2, respectively. Therefore, the chance that a wrong combinatoric yields solutions is enhanced when, for example, Δm_{YX} is close to the correct value of Δm_{XN} . When the two mass differences are close to each other, the turning point is smeared. Nonetheless, with 2000 events after cuts, the errors obtained for the masses are similar to those obtained for Point I.

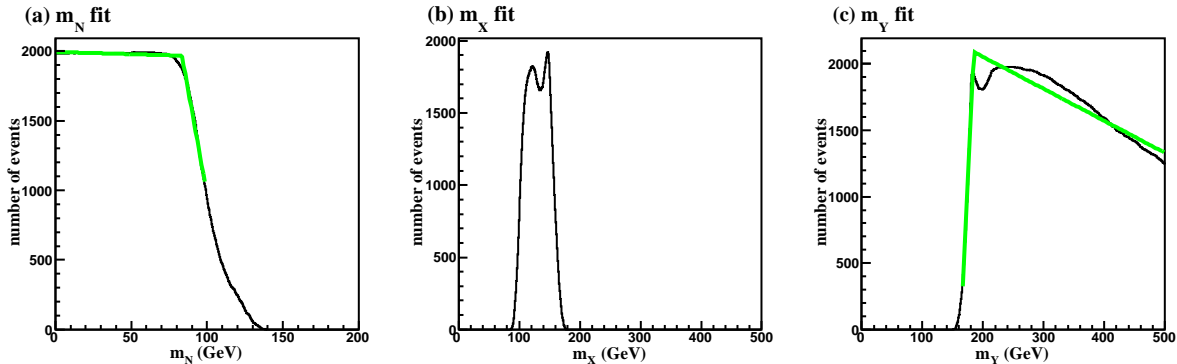


Figure 12: One-dimensional fits for mass point $\{180.8, 147.1, 85.2\}$ GeV.

5.2 Small LSP mass

Another interesting case is that of m_N being zero or very small. As for the previous case, we have arbitrarily used a sample of 2000 events after cuts. Because the one-dimensional fits proceed in the direction of increasing masses, we will miss the correct masses even when we start from $m_N = 0$. Since we always fit the m_N plot to two line segments, it will never yield $m_N = 0$. However, we can distinguish this case by looking at the peak number of events in the m_X fits. For example, considering mass point $\{199.4, 100.0, 0.1\}$ GeV (which we call Point III), we start from $m_X = 80.0$ and $m_N = 0.0$ and fit the masses in the order: $m_Y \rightarrow m_X \rightarrow m_N$. The first few fits yield

$$\{205.0, 80.0, 0\} \rightarrow \{205.0, 101.5, 0\} \rightarrow \{205.0, 101.5, 24.6\} \rightarrow \dots$$

After only two steps, the Y and X masses are adjusted close to the correct values. Examining the peak number of events in the m_X fits (Fig. 13), we find that the number is maximized in the first m_X fit. This is clearly different from previous cases where the number of events always increases for the first few m_X fits (see Fig. 7 b), and indicates that m_N is near zero.

5.3 The SPS1a Point

It is desirable to compare directly to the results obtained by others for the SPS1a SUSY parameter point. We perform the analysis using the same $4\mu\tilde{\chi}_1^0\tilde{\chi}_1^0$ final state that we have been considering. For the usual SPS1a mSUGRA inputs (see Appendix B) the masses for $Y = \tilde{\chi}_2^0$, $X = \tilde{\mu}_R$ and $N = \tilde{\chi}_1^0$ (from ISAJET 7.75) are 180.3 GeV, 142.5 GeV and 97.4 GeV, respectively. This is a more difficult case than Point I considered earlier due to the fact that the dominant decay of the $\tilde{\chi}_2^0$ is $\tilde{\chi}_2^0 \rightarrow \tau\tilde{\tau}_1$. The branching ratio

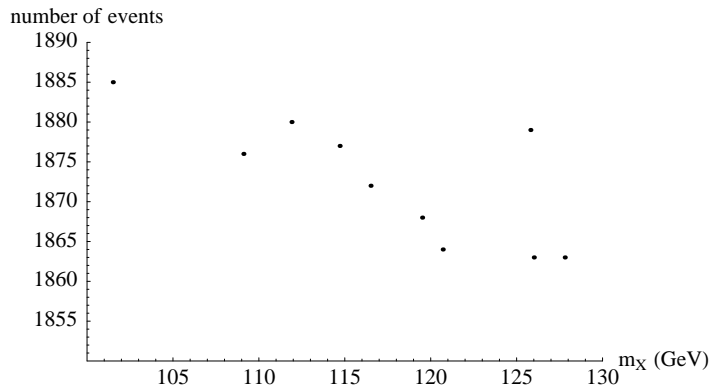


Figure 13: Peak number of events in m_X fits for mass point $\{199.4, 100.0, 0.1\}$ GeV.

for $\tilde{\chi}_2^0 \rightarrow \mu\tilde{\mu}_R$ is such as to leave only about 1200 events in the $4\mu\tilde{\chi}_1^0\tilde{\chi}_1^0$ final state after $L = 300 \text{ fb}^{-1}$ of accumulated luminosity. Cuts reduce the number of events further to about 425. This is too few for our technique to be as successful as for the earlier considered cases. After including combinatorics and resolution we obtain:

$$m_Y = 188 \pm 12 \text{ GeV}, \quad m_X = 151 \pm 14 \text{ GeV}, \quad m_N = 100 \pm 13 \text{ GeV}. \quad (5.1)$$

In Fig. 14, we give an SPS1a plot analogous to Fig. 8. Errors are determined by generating many such plots for different samples of 425 events. Note the vertical scale. The change in the number of events as one varies m_N is quite small for small event samples and this is what leads to the larger errors in this case.

In principle, we must also take into account the fact that the $\tilde{\chi}_2^0 \rightarrow \tau\tilde{\tau}_1$ decays provide a background to the purely muonic final state. The dominant decay $\tilde{\chi}_2^0 \rightarrow \tau\tilde{\tau}_1$ has a branching ratio that is a factor of ~ 14 times larger than that for $\tilde{\chi}_2^0 \rightarrow \ell\tilde{\ell}_R$.⁴ The $\tilde{\tau}_1$ will then decay to $\tau\tilde{\chi}_1^0$. If both τ 's then decay to $\mu\nu\bar{\nu}$, then $\tilde{\chi}_2^0 \rightarrow \tau\tilde{\tau}_1$ events will be likely to contaminate the $\tilde{\chi}_2^0 \rightarrow \mu\tilde{\mu}_R$ sample. Fortunately, this contamination is not huge. The relevant effective branching ratios for $\tilde{\chi}_2^0\tilde{\chi}_2^0 \rightarrow \tau\tilde{\tau}_1\tau\tilde{\tau}_1 \rightarrow 4\mu\tilde{\chi}_1^0\tilde{\chi}_1^0$ and $\tilde{\chi}_2^0\tilde{\chi}_2^0 \rightarrow \tau\tilde{\tau}_1\mu\tilde{\mu}_R \rightarrow 4\mu\tilde{\chi}_1^0\tilde{\chi}_1^0$ are

$$\left[\frac{BR(\tilde{\chi}_2^0 \rightarrow \tau\tilde{\tau}_1 \rightarrow \tau\tau\tilde{\chi}_1^0 \rightarrow \mu\mu 4\nu\tilde{\chi}_1^0)}{BR(\tilde{\chi}_2^0 \rightarrow \mu\tilde{\mu}_R \rightarrow \mu\mu\tilde{\chi}_1^0)} \right]^2 \sim [14 \times (0.174)^2]^2 \sim 0.18 \quad (5.2)$$

and

$$2 \left[\frac{BR(\tilde{\chi}_2^0 \rightarrow \tau\tilde{\tau}_1 \rightarrow \tau\tau\tilde{\chi}_1^0 \rightarrow \mu\mu 4\nu\tilde{\chi}_1^0)}{BR(\tilde{\chi}_2^0 \rightarrow \mu\tilde{\mu}_R \rightarrow \mu\mu\tilde{\chi}_1^0)} \right] \sim 0.85, \quad (5.3)$$

⁴This is, of course, due to the fact that $\tilde{\chi}_2^0$ prefers to couple to left-handed slepton components, which are significant for the $\tilde{\tau}_1$.

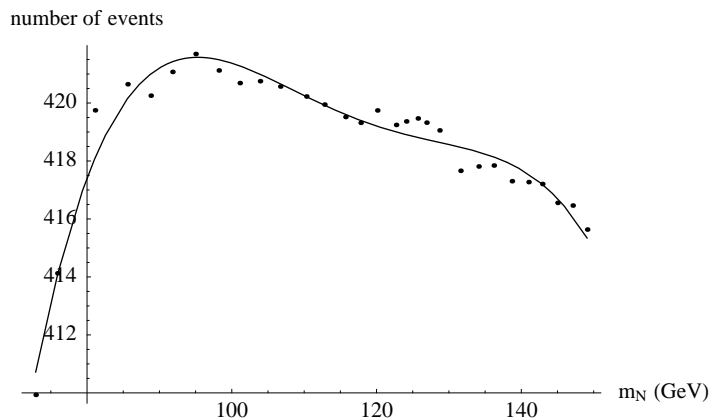


Figure 14: Fitted number of events at the turning point as a function of m_N for the fits for the SPS1a case.

respectively. The contamination levels from these backgrounds are further reduced by factors of ~ 5 for the $\tilde{\chi}_2^0 \tilde{\chi}_2^0 \rightarrow \tau \tilde{\tau}_1 \tau \tilde{\tau}_1$ final state and by ~ 2 for the $\tilde{\chi}_2^0 \tilde{\chi}_2^0 \rightarrow \tau \tilde{\tau}_1 \mu \tilde{\mu}_R$ final state after imposing the simple cuts of Eq. (4.1) (due to the softer nature of the μ 's coming from the τ decays), implying contamination at about the 3.6% and 40% levels, respectively. Clearly, it is important to reduce this level of contamination given that $m_{\tilde{\tau}_1}$ is smaller than $m_{\tilde{\mu}_R}$ by about 15 GeV and so, to the extent that events containing $\tilde{\chi}_2^0 \rightarrow \tau \tilde{\tau}_1$ decays remain in our sample, they might contribute additional structures to our plots of number of events vs. mass. This reduction can be accomplished on a statistical basis using a further trick analogous to that discussed (but not, we believe, actually employed) in Ref. [10]. They note that the decay sequences $\tilde{\chi}_2^0 \rightarrow \mu^- e^+ \tilde{\chi}_1^0$ and $\tilde{\chi}_2^0 \rightarrow \mu^+ e^- \tilde{\chi}_1^0$ are unique to $\tilde{\chi}_2^0 \rightarrow \tau \tilde{\tau}_1$. Thus, when considering just the one-sided decay chain situation one can subtract off (on a statistical basis, *i.e.* after many events) the $\tilde{\chi}_2^0 \rightarrow \tau \tilde{\tau}_1$ background by

$$N(\tilde{\chi}_2^0 \rightarrow \mu \tilde{\mu}_R \rightarrow \mu \mu \tilde{\chi}_1^0) = N(\tilde{\chi}_2^0 \rightarrow \mu \mu \tilde{\chi}_1^0) - N(\tilde{\chi}_2^0 \rightarrow \mu e \tilde{\chi}_1^0), \quad (5.4)$$

where N is the number of ‘solved’ events as a function of one of the unknown on-shell masses. In our case, where both chain decays are considered simultaneously, we have $4\mu \tilde{\chi}_1^0 \tilde{\chi}_1^0$ states arising from $\tilde{\chi}_2^0 \tilde{\chi}_2^0 \rightarrow \tau^\pm \tilde{\tau}_1^\mp \tau^\pm \tilde{\tau}_1^\mp$ decays and $\tilde{\chi}_2^0 \tilde{\chi}_2^0 \rightarrow \tau^\pm \tilde{\tau}_1^\mp \mu^\pm \tilde{\mu}_R^\mp$ decays in addition those from our $\tilde{\chi}_2^0 \tilde{\chi}_2^0 \rightarrow \mu^\pm \tilde{\mu}_R^\mp \mu^\pm \tilde{\mu}_R^\mp$ signal. To subtract off the background SUSY events from the former two decay chains, we can employ the following subtraction

(where the initial $\tilde{\chi}_2^0\tilde{\chi}_2^0$ and final $\tilde{\chi}_1^0\tilde{\chi}_1^0$ are implicit)

$$\begin{aligned}
N(\mu^\pm\tilde{\mu}_R^\mp\mu^\pm\tilde{\mu}_R^\mp \rightarrow \mu^+\mu^-\mu^+\mu^-) &= N(\mu^+\mu^-\mu^+\mu^-) - N(e^+\mu^-\mu^+\mu^-) + N(e^+e^+\mu^-\mu^-) \\
&= N(\mu^+\mu^-\mu^+\mu^-) - \frac{1}{4} \left[N(e^+\mu^-\mu^+\mu^-) + N(e^-\mu^+\mu^-\mu^+) \right. \\
&\quad \left. + N(\mu^+e^-e^+e^-) + N(\mu^-e^+e^-e^+) \right] \\
&\quad + \frac{1}{2} \left[N(e^+e^+\mu^-\mu^-) + N(e^-e^-\mu^+\mu^+) \right].
\end{aligned} \tag{5.5}$$

where the latter form is likely to have smaller statistical error. An experimental indicator of the sensitivity to statistics could be gained by examining the different possible equivalent subtractions, of which only two are indicated above. If one were happy to ignore the 3.6% contamination from $\tilde{\chi}_2^0\tilde{\chi}_2^0 \rightarrow \tau^\pm\tilde{\tau}_1^\mp\tau^\pm\tilde{\tau}_1^\mp$ decays one could then use a simpler form to subtract off the dominant contamination from $\tilde{\chi}_2^0\tilde{\chi}_2^0 \rightarrow \tau^\pm\tilde{\tau}_1^\mp\mu^\pm\tilde{\mu}_R^\mp$ decays, namely

$$\begin{aligned}
N(\mu^\pm\tilde{\mu}_R^\mp\mu^\pm\tilde{\mu}_R^\mp \rightarrow \mu^+\mu^-\mu^+\mu^-) &\sim N(\mu^+\mu^-\mu^+\mu^-) - N(e^+\mu^-\mu^+\mu^-) \\
&\sim N(\mu^+\mu^-\mu^+\mu^-) - \frac{1}{2} \left[N(e^+\mu^-\mu^+\mu^-) + N(e^-\mu^+\mu^-\mu^+) \right].
\end{aligned} \tag{5.6}$$

We have not actually performed this kind of analysis using any of the possible subtractions to see how well we do, but we expect that the net background contamination will be equivalent to $B/S \lesssim 0.1$, a level for which our techniques work very well and the errors quoted earlier for the SPS1a point using the 4μ final state will not be increased by very much.

Of course, the same analysis as performed for the 4μ final state can also be used for the $2\mu 2e$ and $4e$ final states. Combinatorics are less of an issue for the $2\mu 2e$ final state than for the 4μ and $4e$ final states. The $4e$ -channel event number is essentially the same as the 4μ -channel event number and the $2\mu 2e$ -channel event number is roughly twice as large. Combining all channels (as appropriate if the \tilde{e} has mass very close to the $\tilde{\mu}$, as predicted by the model), one obtains a total of about 1700 events and ~ 5 GeV errors for our $m_{\tilde{\chi}_2^0}$, $m_{\tilde{e}}$ and $m_{\tilde{\chi}_1^0}$ determinations.

Of course, as the observant reader may have noticed, to get 1700 events requires running at high luminosity, whereas the simulations referenced so far have employed the p_T^{miss} resolution expected at low-luminosity running. The p_T^{miss} low-luminosity resolution is about 5.8 GeV and that at high luminosity is about 11.6 GeV. However, we have argued that perhaps one is not all that sensitive to this resolution when considering

a large collection of events and looking for the location of an edge in the number of reconstructed events. We have used the SPS1a point to test this hypothesis by repeating our analysis using high-luminosity running resolutions.

The results confirm our hypothesis. First, the worse resolution results in our accepting somewhat more events than previously, roughly 480 events (this is the average for the 10 Monte Carlo “experiments” employed) in the 4μ channel for the same cuts (and $L = 300 \text{ fb}^{-1}$). The resulting mass determinations obtained using the 10 independent Monte Carlo experiments are

$$m_Y = 187 \pm 10 \text{ GeV}, \quad m_X = 151 \pm 10 \text{ GeV}, \quad m_N = 98 \pm 9 \text{ GeV}, \quad (5.7)$$

where the errors are, as always, rms errors. In short, we get even smaller errors than for low-luminosity running. After combining the 4μ , $4e$ and $2\mu 2e$ channels assuming $\tilde{e}-\tilde{\mu}$ degeneracy our mass determination errors are slightly above 4 GeV.

6. Summary and Discussion

For any theory that simultaneously provides a solution of the hierarchy problem and a dark matter particle as a result of a symmetry guaranteeing its stability, implying pair production of its heavier partners, the relevant LHC events will be ones in which the heavier partners are pair produced, with each chain decaying down to largely visible SM particles and the dark matter particle, which we denote by N . In many interesting cases, towards the end of each such chain 2 visible SM particles emerge along with the invisible dark matter particle, *e.g.* $Y \rightarrow \mu X \rightarrow \mu\mu N$, with the preceding parts of the decay chains giving rise to jets. In other cases, two Y particles are directly produced and initiate 2 such chain decays. In this paper, we have developed a highly effective technique for using the kinematic information in a typical event containing two $Y \rightarrow \mu X \rightarrow \mu\mu N$ decay chains to determine not just the mass differences in the chain decay, but also the absolute mass scale, using only the measured μ momenta and overall visible and missing transverse momenta. Since we use purely kinematic information, our mass determination does not require any assumptions regarding particle spins, shapes of distributions, cross section and so forth. Further, our procedure works whether or not we know the topology of each of the chains that precedes the $Y \rightarrow \mu X \rightarrow \mu\mu N$ stage. This can be a big advantage. For example, in the supersymmetry context this allows us to combine \tilde{g} and \tilde{q} initiated chains.

In our study, we have included resolution smearing for muon momenta and missing momentum as incorporated in the ATLFast simulation program. We have also included full combinatorics appropriate to the $jets + 4\mu NN$ final state. Assuming of

order 2000 events after cuts and ATLFAST resolutions appropriate to low-luminosity running, we have found statistical errors of order 4 GeV for the individual Y , X and N masses, assuming a reasonable background to signal ratio, $B/S \lesssim 0.5$. There is also a small systematic bias in the masses extracted. However, this bias can be removed using Monte Carlo simulations once the masses are fairly well known. The appropriate procedure is described in Sec. 4.1. We have not yet performed the associated highly computer intensive procedure, but believe that the systematic biases can be reduced below 1 GeV (a residual that we think might arise from possible model dependence of the kinematic distributions).

As a particular point of comparison with the many earlier studies that use the mass-edge technique, we have examined the standard SPS1a point. Following our procedure we are left with about 1920 events (averaging over 10 Monte Carlo “experiments”) in the $jets + 4\mu$, $jets + 2e + 2\mu$ and $jets + 4e$ channels after cuts assuming an integrated luminosity of 300 fb^{-1} and employing resolutions appropriate to high-luminosity running. The errors on $m_{\tilde{\chi}_2^0}$, $m_{\tilde{\tau}}$ and $m_{\tilde{\chi}_1^0}$ are all between 4 GeV and 5 GeV if $\tilde{\mu}$ and \tilde{e} mass degeneracy is assumed. The previous mass-edge studies make this same assumption and employ *all* the final SM particles of the full $\tilde{g} \rightarrow \tilde{b}\tilde{b} \rightarrow b\tilde{b}\tilde{\chi}_2^0 \rightarrow b\tilde{b}\tilde{\ell}\tilde{\ell} \rightarrow b\tilde{b}\tilde{\ell}\tilde{\ell}\tilde{\chi}_1^0$ decay chain but examine only one chain at a time. Only one of these mass-edge studies claims an accuracy ($\sim \pm 5$ GeV for $m_{\tilde{\chi}_2^0}$, $m_{\tilde{\tau}}$ and $m_{\tilde{\chi}_1^0}$) for the same channels and integrated luminosity that is competitive with the small error we obtain.

By comparing the SPS1a results obtained for high-luminosity resolutions to those for this same point using low-luminosity resolutions (as summarized in the previous section) we found the important result that the accuracy of our mass determinations was very little influenced by whether or not we employed low- or high-luminosity resolution for p_T^{miss} , the latter being essentially twice the former. That our ability to locate the “edge” in a plot of the number of reconstructed events, N_{evt} , as a function of the test value of, say, $m_{\tilde{\chi}_1^0}$, is not noticeably affected by a factor of two deterioration in resolution for p_T^{miss} is a sign of the robustness of our approach.

Accuracies of order 4 – 5 GeV for the masses of new-physics particles will yield an accurate determination of the TeV-scale underlying parameters of the associated new physics model. The latter accuracy will, in turn, typically yield reasonably precise evolved values for the model parameters at any higher scale (*e.g.* the coupling constant unification scale in SUSY) where they might follow a meaningful pattern that would determine the more fundamental structure of the new physics theory. Further, an accuracy of order 4 – 5 GeV for the dark matter particle mass will in many cases allow a sufficiently accurate calculation for the dark matter density from annihilations in the early universe as to allow a meaningful comparison with the very accurate observed value. In some cases, the dark matter particle coannihilates with another particle of

only slightly larger mass. We will be exploring the extent to which the mass of the coannihilation partner could be determined in such a situation. For the moment, we can only claim the 4 – 5 GeV kind of error on individual masses when mass differences are reasonably substantial (and the number of events after cuts is of order 1700 to 2000).

A ‘fun’ example that we hope our experimental colleagues will pursue is to employ our method for determining the mass scales for the top and W simultaneously in the $t\bar{t}$ di-lepton decay topology. Or, given that the W mass is already quite well-known, they could impose this additional constraint in our context and get an excellent t mass determination.

The heart of our technique is the fact that by considering both decay chains in a typical LHC event together, a choice for the chain decay masses $\mathcal{M} = \{m_Y, m_X, m_N\}$ (see Fig. 2) in combination with the measured momenta of the 4 visible and measurable SM particles emitted in the two chains implies a discrete (sometimes even unique) set of three momenta for the two final state N 's. (One is solving a quartic equation.) Conversely, if we have already used our procedure to determine to good precision the $\mathcal{M} = \{m_Y, m_X, m_N\}$ masses, we can invert the process. For each event, we can input the known masses and obtain a set of discrete choices for the momenta, \vec{p}_N and $\vec{p}_{N'}$, of the final invisible particles. For each discrete choice, the 4-momenta of all particles in the decay chains are then determined. These 4-momenta can then be input to a given model (with definite spins for the Y, X, N and definite decay correlations and so forth). One can then test the experimental distributions (*e.g.* of correlation angles, of masses constructed from the visible SM particles, and so forth) against predictions obtained for the model using a Monte Carlo. Presumably, this will provide strong discrimination between different models that have the same already-determined chain decay masses. The only question is to what extent the possibility of more than one discrete solution for each event will confuse the distributions obtained from the Monte Carlo.

Conversely, it is clear that determining the spins of all the particles in a chain of decays can be difficult without a relatively precise *purely-kinematic* determination of the masses. In particular, we expect that angular correlations and the like (obtained from Monte Carlos that assume a particular model including spins) will be strongly influenced by the masses. Confusion between two different models with differing spins and masses can be anticipated in the absence of an independent purely-kinematical determination of the masses.

Overall, we claim that our techniques provide some powerful new tools for doing precision physics at the LHC in an environment where new physics events contain invisible particles of unknown mass. We hope the experimental community will pursue the approaches we have analyzed. We do not anticipate that fully realistic simulations

will lead to significantly larger errors for new particle masses than those we have found, but it is clearly important to verify that this is the case.

Acknowledgments

This work was supported in part by U.S. Department of Energy grant No. DE-FG03-91ER40674. JFG and HCC thank the Aspen Center for Physics where a portion of this work was performed.

Appendices

A. Solution Procedure

To determine whether a given event with the topology of Fig. 2 is consistent with a given mass hypothesis, we proceed as follows. We envision the process of $pp \rightarrow (135) + (246)$, followed by $(135) \rightarrow 5 + (31)$ and $(246) \rightarrow 6 + (42)$, which in turn is followed by $(31) \rightarrow 3 + 1$ and $(42) \rightarrow 4 + 2$. (The objects in (...) are to be thought of as single on-shell particles: in the notation of Fig. 2, $(135) = Y$, $(246) = Y'$, $(13) = X$, $(24) = X'$, $1 = N$ and $2 = N'$.) We will be assuming input values for m_{135}^2 , m_{246}^2 , m_{13}^2 , m_{24}^2 , m_1^2 and m_2^2 , assuming $m_{135}^2 = m_{246}^2$, $m_{13}^2 = m_{24}^2$ and $m_1^2 = m_2^2$. The cross section takes the form

$$d\sigma = \frac{1}{2s(2\pi)^8} \int dx_1 dx_2 |\mathcal{M}|^2 f(x_1) f(x_2) \frac{d^3\vec{p}_5}{2E_5} \frac{d^3\vec{p}_6}{2E_6} \frac{d^3\vec{p}_3}{2E_3} \frac{d^3\vec{p}_4}{2E_4} \frac{d^3\vec{p}_1}{2E_1} \frac{d^3\vec{p}_2}{2E_2} \times \delta^4 [x_1 p_A + x_2 p_B - (p_1 + p_2 + p_3 + p_4 + p_5 + p_6)] \quad (\text{A.1})$$

We first convert

$$dx_1 dx_2 = \frac{2}{s} dE_{tot} dp_{tot}^z, \quad (\text{A.2})$$

introduce on-shell masses for the intermediate particles, and introduce on-shell δ functions for the invisible particles 1 and 2 to yield

$$\begin{aligned}
d\sigma &= \frac{1}{4(2\pi)^8} \int dE_{tot} dp_{tot}^z dm_{135}^2 dm_{246}^2 dm_{31}^2 dm_{24}^2 |\mathcal{M}|^2 f(x_1) f(x_2) \frac{d^3\vec{p}_5}{2E_5} \frac{d^3\vec{p}_6}{2E_6} \frac{d^3\vec{p}_3}{2E_3} \frac{d^3\vec{p}_4}{2E_4} \\
&\quad \times d^4p_1 \delta(p_1^2 - m_1^2) d^4p_2 \delta(p_2^2 - m_2^2) \\
&\quad \times \delta^4 [x_1 p_A + x_2 p_B - (p_1 + p_2 + p_3 + p_4 + p_5 + p_6)] \\
&\quad \times \delta[(p_1 + p_3 + p_5)^2 - m_{135}^2] \delta[(p_2 + p_4 + p_6)^2 - m_{246}^2] \\
&\quad \times \delta[(p_3 + p_1)^2 - m_{31}^2] \delta[(p_2 + p_4)^2 - m_{42}^2] \\
&= \frac{1}{4(2\pi)^8} \int dp_{tot}^z dm_{135}^2 dm_{246}^2 dm_{31}^2 dm_{24}^2 |\mathcal{M}|^2 f(x_1) f(x_2) \frac{d^3\vec{p}_5}{2E_5} \frac{d^3\vec{p}_6}{2E_6} \frac{d^3\vec{p}_3}{2E_3} \frac{d^3\vec{p}_4}{2E_4} \\
&\quad \times d^4p_1 \delta(p_1^2 - m_1^2) d^4p_2 \delta(p_2^2 - m_2^2) \\
&\quad \times \delta[(p_1 + p_3 + p_5)^2 - m_{135}^2] \delta[(p_2 + p_4 + p_6)^2 - m_{246}^2] \\
&\quad \times \delta[(p_3 + p_1)^2 - m_{31}^2] \delta[(p_2 + p_4)^2 - m_{42}^2]
\end{aligned} \tag{A.3}$$

where in the last step we eliminated $d^3\vec{p}_2$ using the 3-momentum conservation part of the δ^4 function and eliminated E_{tot} using the energy part of the δ^4 function. For fixed values of the unknown masses, we end up with the 4 unknowns of p_{tot}^z and \vec{p}_1 , to be solved for using the 4 on-shell δ functions. We will now define

$$p_{vis} \equiv p_3 + p_5 + p_4 + p_6. \tag{A.4}$$

Assuming no transverse momentum for the $Y + Y' = 1 + 2 + 3 + 4 + 5 + 6$ system, we then have

$$\begin{aligned}
p_1 \cdot p_3 &= E_1 E_3 - p_1^z p_3^z - p_1^y p_3^y - p_1^x p_3^x \\
p_2 \cdot p_4 &= E_2 E_4 - (p_{tot}^z - p_{vis}^z - p_1^z) p_4^z - (-p_{vis}^y - p_1^y) p_4^y - (-p_{vis}^x - p_1^x) p_4^x \\
p_1 \cdot p_5 &= E_1 E_5 - p_1^z p_5^z - p_1^y p_5^y - p_1^x p_5^x \\
p_2 \cdot p_6 &= E_2 E_6 - (p_{tot}^z - p_{vis}^z - p_1^z) p_6^z - (-p_{vis}^y - p_1^y) p_6^y - (-p_{vis}^x - p_1^x) p_6^x.
\end{aligned} \tag{A.5}$$

(Transverse momentum for the $Y + Y'$ system can, and must, be included in the obvious way. We compute it as the negative of the sum of the observed momenta of particles 3, 4, 5 and 6 and the missing momentum.) We next combine the last two δ functions and consider the requirement (again, recall that we are assuming some input mass values for the intermediate on-shell particle masses)

$$2p_3 \cdot p_1 - 2p_2 \cdot p_4 + \Delta_{2b} \equiv G_1 = 0, \tag{A.6}$$

where

$$\Delta_{2b} \equiv m_3^2 + m_1^2 - m_{31}^2 + m_{42}^2 - m_2^2 - m_4^2. \quad (\text{A.7})$$

Similarly we combine the 135 and 246 δ functions to obtain

$$2p_1 \cdot p_5 - 2p_2 \cdot p_6 + \Delta_{3b} \equiv G_2 = 0, \quad (\text{A.8})$$

where

$$\Delta_{3b} \equiv m_{31}^2 + m_5^2 - m_{531}^2 + m_{642}^2 - m_{42}^2 - m_6^2 + 2p_3 \cdot p_5 - 2p_4 \cdot p_6. \quad (\text{A.9})$$

Of course, m_5^2 and m_6^2 are measured experimentally (and are typically small unless one is a W or Z), and $2p_3 \cdot p_5$ and $2p_4 \cdot p_6$ are also computable from the experimental event. Further, we are assuming input values for m_{31}^2 , m_{42}^2 , m_{531}^2 and m_{642}^2 . The above is a convenient organization, since $\Delta_{2b} = 0$ and Δ_{3b} reduces to just momenta dot products when the two decay chains are identical.

We now implement directly the m_{31}^2 and m_{531}^2 δ functions.

$$m_{31}^2 - m_1^2 - m_3^2 - 2p_1 \cdot p_3 \equiv \Delta_{31}^2 - 2p_1 \cdot p_3 \equiv G_3 = 0, \quad (\text{A.10})$$

and

$$m_{531}^2 - m_{31}^2 - m_5^2 - 2p_3 \cdot p_5 - 2p_1 \cdot p_5 \equiv \Delta_{531} - 2p_1 \cdot p_5 \equiv G_4 = 0, \quad (\text{A.11})$$

where again $2p_3 \cdot p_5$ is determined experimentally and the masses are being input.

We now solve these 4 equations for the 4 unknowns of p_{tot}^z , p_1^z , p_1^y , and p_1^x . We write the solutions in the form:

$$\begin{aligned} p_1^x &= c_{xe1}E_1 + c_{xe2}E_2 + c_x \\ p_1^y &= c_{ye1}E_1 + c_{ye2}E_2 + c_y \\ p_1^z &= c_{ze1}E_1 + c_{ze2}E_2 + c_z \\ p_{tot}^z &= c_{zte1}E_1 + c_{zte2}E_2 + c_{zt} \end{aligned} \quad (\text{A.12})$$

where the c 's above are somewhat complicated functions of the masses, energies and momenta of the visible particles, 3, 4, 5, and 6. The Jacobian for the variable change $p_1^x, p_1^y, p_1^z, p_{tot}^z \rightarrow G_1, G_2, G_3, G_4$ is easily computed as

$$\begin{aligned} J &= 16 \left[-p_3^z p_4^z p_5^y p_6^x + p_3^y p_4^z p_5^z p_6^x + p_3^z p_4^z p_5^x p_6^y - p_3^x p_4^z p_5^z p_6^y \right. \\ &\quad \left. - p_3^z p_4^y p_5^x p_6^z + p_3^z p_4^x p_5^y p_6^z - p_3^y p_4^x p_5^z p_6^z + p_3^x p_4^y p_5^z p_6^z \right] \end{aligned} \quad (\text{A.13})$$

It is a function only of observed momenta. For the next stage, we combine the expressions of Eq. (A.12) with

$$p_2^x = -p_{vis}^x - p_1^x, \quad p_2^y = -p_{vis}^y - p_1^y, \quad p_2^z = p_{tot}^z - p_{vis}^z - p_1^z, \quad (\text{A.14})$$

and solve the equations for the on-shell δ functions for p_1 and p_2 (the invisible particles)

$$0 = E_1^2 - (p_1^x)^2 - (p_1^y)^2 - (p_1^z)^2 - m_1^2 \quad (\text{A.15})$$

$$0 = E_2^2 - (p_2^x)^2 - (p_2^y)^2 - (p_2^z)^2 - m_2^2 \quad (\text{A.16})$$

for E_1 and E_2 . For convenience, we rewrite Eqs. (A.15) and (A.16) in the respective forms:

$$a_{11}E_1^2 + a_{12}E_1E_2 + a_{22}E_2^2 + a_1E_1 + a_2E_2 + a \equiv F_A = 0 \quad (\text{A.17})$$

$$b_{11}E_1^2 + b_{12}E_1E_2 + b_{22}E_2^2 + b_1E_1 + b_2E_2 + b \equiv F_B = 0 \quad (\text{A.18})$$

where the a_{ij} , b_{ij} , a_i , b_i as well as a and b are functions of the c 's, m_1^2 , m_2^2 and the components of \vec{p}_{vis} . We now take

$$F_A - \frac{a_{11}}{b_{11}} \times F_B = 0 \quad (\text{A.19})$$

and solve the resulting linear equation for E_1 to obtain

$$E_1 = \frac{a_{11} b - a b_{11} - a_2 b_{11} E_2 + a_{11} b_2 e_2 - a_{22} b_{11} E_2^2 + a_{11} b_{22} E_2^2}{-a_{11} b_1 + a_1 b_{11} + a_{12} b_{11} E_2 - a_{11} b_{12} E_2} \quad (\text{A.20})$$

We now substitute this result into Eq. (A.17) to obtain the final quartic equation for E_2 of form

$$AE_2^4 + BE_2^3 + CE_2^2 + DE_2 + E = 0, \quad (\text{A.21})$$

where A , B , C , D and E are functions of the a_{ij} , b_{ij} , a_i , b_i , a and b . We then employ a standard computer subroutine for obtaining the 4 roots of this quartic equation. For typical input visible momenta, some of the roots will be acceptable real solutions and some will be imaginary. We retain all real solutions. (The Jacobian for the $F_A, F_B \rightarrow E_1, E_2$ transformation is easily computed.) Once real values for E_1 and E_2 are obtained these can be substituted into Eq. (A.12) to determine the 3-vector components of p_1 and the z component of p_{tot} . The components of p_2 are then obtained by momentum conservation. At this point, the invisible 4-momenta are fully determined and could potentially be employed in a model matrix element.

B. SUSY points

In this appendix, we give details regarding the SUSY points simulated.

B.1 Point I

We input low-scale parameters of

$$\begin{aligned} \mu = +300 \text{ GeV}, \quad \tan \beta = 10, \quad (\widetilde{M}_1, \widetilde{M}_2, \widetilde{M}_3) = (90, 300, 500) \text{ GeV} \\ \widetilde{m}_L^{(1,2,3)} = \widetilde{m}_E^{(3)} = 1000 \text{ GeV}, \quad \widetilde{m}_E^{(1,2)} = 120 \text{ GeV} \\ \widetilde{m}_Q^{(1,2)} = 400 \text{ GeV}, \quad \widetilde{m}_{U,D}^{(1,2)} = 300 \text{ GeV}, \quad \widetilde{m}_Q^{(3)} = \widetilde{m}_{U,D}^{(3)} = 1000 \text{ GeV} \end{aligned} \quad (\text{B.1})$$

where the \widetilde{m} 's are the soft slepton and squark masses, and the \widetilde{M} 's are the gaugino masses. L and Q refer to the slepton and squark $SU(2)_W$ doublets and E , U and D refer to the slepton and squark singlets. Superscripts give the generations. The decay chain of interest is

$$\widetilde{q}_L \rightarrow q\widetilde{\chi}_2^0 \quad \widetilde{\chi}_2^0 \rightarrow \mu\widetilde{\mu}_R, \quad \widetilde{\mu}_R \rightarrow \mu\widetilde{\chi}_1^0. \quad (\text{B.2})$$

Using the input soft parameters as specified above and SPheno 2.2.3 [22], the sparticle masses of relevance for our discussion are (all in GeV):

$$\begin{aligned} m_{\widetilde{g}} \sim 524, \quad m_{\widetilde{d}_L, \widetilde{s}_L} \sim 438, \quad m_{\widetilde{u}_L, \widetilde{c}_L} \sim 431 \\ m_{\widetilde{\chi}_2^0} \sim 246.6, \quad m_{\widetilde{\mu}_R} \sim 128.4, \quad m_{\widetilde{\chi}_1^0} \sim 85.3 \end{aligned} \quad (\text{B.3})$$

For this point, the net cross section available is

$$\sigma \left(pp \rightarrow \sum_{q,q'=u,d,c,s} \widetilde{q}_L \widetilde{q}_L + \sum_{q,q'=u,d,c,s} \widetilde{q}_L \overline{\widetilde{q}}_L + \sum_{q,q'=u,d,c,s} \overline{\widetilde{q}}_L \overline{\widetilde{q}}_L \right) \sim 2.9 \times 10^4 \text{ fb}, \quad (\text{B.4})$$

coming from all sources including gg fusion, $u_L u_L$ fusion, *etc.* The branching ratios relevant to the particular decay chain we examine are

$$\begin{aligned} BR(\widetilde{q}_L \rightarrow q\widetilde{\chi}_2^0) \sim 0.27 \quad (q = u, d, c, s) \\ BR(\widetilde{\chi}_2^0 \rightarrow \widetilde{\mu}_R^\pm \mu^\mp) \sim 0.124 \\ BR(\widetilde{\mu}_R^\pm \rightarrow \mu^\pm \widetilde{\chi}_1^0) = 1. \end{aligned} \quad (\text{B.5})$$

The net effective branching ratio for the double decay chain is

$$BR(\widetilde{q}_L \widetilde{q}_L \rightarrow 4\mu\widetilde{\chi}_1^0\widetilde{\chi}_1^0) \sim (0.27)^2 \times (0.124)^2 \sim 1.12 \times 10^{-3} \quad (\text{B.6})$$

for any one \widetilde{q}_L choice. The effective cross section for the $4\mu\widetilde{\chi}_1^0\widetilde{\chi}_1^0$ final state is then

$$\sigma(4\mu\widetilde{\chi}_1^0\widetilde{\chi}_1^0) \sim 2.9 \times 10^4 \text{ fb} \times 1.12 \times 10^{-3} \sim 32.5 \text{ fb}. \quad (\text{B.7})$$

For an integrated luminosity of $L = 90 \text{ fb}^{-1}$, this gives us 2900 $4\mu\widetilde{\chi}_1^0\widetilde{\chi}_1^0$ events before any cuts are applied. After cuts, we are left with about 1900 events.

B.2 Point II

Point II is defined by the following input low-scale SUSY parameters:

$$\begin{aligned} \mu = +300 \text{ GeV}, \quad \tan \beta = 10, \quad (\widetilde{M}_1, \widetilde{M}_2, \widetilde{M}_3) = (90, 200, 500) \text{ GeV} \\ \widetilde{m}_L^{(1,2,3)} = \widetilde{m}_E^{(3)} = 1000 \text{ GeV}, \quad \widetilde{m}_E^{(1,2)} = 140 \text{ GeV} \\ \widetilde{m}_Q^{(1,2)} = 400 \text{ GeV}, \quad \widetilde{m}_{U,D}^{(1,2)} = 300 \text{ GeV}, \quad \widetilde{m}_Q^{(3)} = \widetilde{m}_{U,D}^{(3)} = 1000 \text{ GeV}. \end{aligned} \quad (\text{B.8})$$

Using SPheno 2.2.3 [22], the relevant chain-decay masses are

$$\{m_Y = m_{\widetilde{\chi}_2^0}, m_X = m_{\widetilde{\mu}_R}, m_N = m_{\widetilde{\chi}_1^0}\} = \{180.8, 147.1, 85.2\} \text{ GeV}. \quad (\text{B.9})$$

However, we do not employ the cross sections and branching ratios predicted by these parameters. Instead, we assume 2000 available experimental points after cuts, close to the 1900 left after cuts in the case of Point I. This allows us to see how errors change in the case where $m_Y - m_X$ is much smaller than in the case of Point I.

B.3 Point III

The masses used in this case are obtained from PYTHIA 1.0.8 [21] using the low-scale parameters

$$\begin{aligned} \mu = +3000 \text{ GeV}, \quad \tan \beta = 10, \quad (\widetilde{M}_1, \widetilde{M}_2, \widetilde{M}_3) = (0.2, 200, 500) \text{ GeV} \\ \widetilde{m}_L^{(1,2,3)} = \widetilde{m}_E^{(3)} = 1000 \text{ GeV}, \quad \widetilde{m}_E^{(1,2)} = 100 \text{ GeV} \\ \widetilde{m}_Q^{(1,2)} = 400 \text{ GeV}, \quad \widetilde{m}_{U,D}^{(1,2)} = 300 \text{ GeV}, \quad \widetilde{m}_Q^{(3)} = \widetilde{m}_{U,D}^{(3)} = 1000 \text{ GeV} \end{aligned} \quad (\text{B.10})$$

yielding

$$\{m_Y = m_{\widetilde{\chi}_2^0}, m_X = m_{\widetilde{\mu}_R}, m_N = m_{\widetilde{\chi}_1^0}\} = \{199.4, 100.0, 0.1\} \text{ GeV}. \quad (\text{B.11})$$

Again, we assume 2000 available experimental points after cuts, close to the 1900 events after cuts obtained for Point I.

B.4 Point IV: SPS1a

For the SPS1a point, we use the GUT-scale mSUGRA inputs of

$$m_{1/2} = 250 \text{ GeV}, \quad m_0 = 100 \text{ GeV}, \quad A_0 = -100 \text{ GeV}, \quad \tan \beta = 10, \quad \mu > 0. \quad (\text{B.12})$$

From ISAJET 7.75, the spectrum is calculated as

$$\begin{aligned} m_{\widetilde{g}} \sim 608 \text{ GeV}, \quad m_{\widetilde{a}_L, \widetilde{s}_L} \sim 571 \text{ GeV}, \quad m_{\widetilde{u}_L, \widetilde{c}_L} \sim 565 \text{ GeV} \\ m_{\widetilde{\chi}_2^0} \sim 180.3 \text{ GeV}, \quad m_{\widetilde{\mu}_R} \sim 142.5 \text{ GeV}, \quad m_{\widetilde{\chi}_1^0} \sim 97.4 \text{ GeV} \quad m_{\widetilde{\tau}_1} \sim 134.7 \text{ GeV} \end{aligned} \quad (\text{B.13})$$

The total effective cross-section including all channels for $\tilde{\chi}_2^0\tilde{\chi}_2^0$ production is about 1 pb. The relevant branching ratios are:

$$BR(\tilde{\chi}_2^0 \rightarrow \tilde{\mu}_R^\pm \mu^\mp) \sim 0.063, \quad BR(\tilde{\mu}_R^\pm \rightarrow \mu^\pm \tilde{\chi}_1^0) = 1. \quad (\text{B.14})$$

For $L = 300 \text{ fb}^{-1}$, this gives 1200 events before any cuts. After cuts, we are left with about 425 events. Errors for the masses given in the text are based upon the latter.

References

- [1] T. Appelquist, H. C. Cheng and B. A. Dobrescu, “Bounds on universal extra dimensions,” *Phys. Rev. D* **64**, 035002 (2001) [arXiv:hep-ph/0012100].
- [2] H. C. Cheng, D. E. Kaplan, M. Schmaltz and W. Skiba, “Deconstructing gaugino mediation,” *Phys. Lett. B* **515**, 395 (2001) [arXiv:hep-ph/0106098]; “Bosonic supersymmetry? Getting fooled at the LHC,” *Phys. Rev. D* **66**, 056006 (2002) [arXiv:hep-ph/0205314].
- [3] H. C. Cheng and I. Low, “TeV symmetry and the little hierarchy problem,” *JHEP* **0309**, 051 (2003) [arXiv:hep-ph/0308199]; “Little hierarchy, little Higgses, and a little symmetry,” *JHEP* **0408**, 061 (2004) [arXiv:hep-ph/0405243].
- [4] K. Agashe and G. Servant, “Warped unification, proton stability and dark matter,” *Phys. Rev. Lett.* **93**, 231805 (2004) [arXiv:hep-ph/0403143].
- [5] E. A. Baltz, M. Battaglia, M. E. Peskin and T. Wizansky, *Phys. Rev. D* **74**, 103521 (2006) [arXiv:hep-ph/0602187].
- [6] I. Hinchliffe, F. E. Paige, M. D. Shapiro, J. Soderqvist and W. Yao, “Precision SUSY measurements at LHC,” *Phys. Rev. D* **55**, 5520 (1997) [arXiv:hep-ph/9610544].
- [7] C. G. Lester and D. J. Summers, “Measuring masses of semi-invisibly decaying particles pair produced at hadron colliders,” *Phys. Lett. B* **463**, 99 (1999) [arXiv:hep-ph/9906349]; A. Barr, C. Lester and P. Stephens, “m(T2): The truth behind the glamour,” *J. Phys. G* **29**, 2343 (2003) [arXiv:hep-ph/0304226].
- [8] H. Bachacou, I. Hinchliffe and F. E. Paige, “Measurements of masses in SUGRA models at LHC,” *Phys. Rev. D* **62**, 015009 (2000) [arXiv:hep-ph/9907518].
- [9] B. C. Allanach, C. G. Lester, M. A. Parker and B. R. Webber, “Measuring sparticle masses in non-universal string inspired models at the LHC,” *JHEP* **0009**, 004 (2000) [arXiv:hep-ph/0007009]. See also C. G. Lester, <http://cdsweb.cern.ch/search.py?sysno=002420651CER>.

- [10] B. K. Gjelsten, D. J. Miller and P. Osland, “Measurement of SUSY masses via cascade decays for SPS1a,” JHEP **0412**, 003 (2004) [arXiv:hep-ph/0410303].
- [11] G. Weiglein *et al.* [LHC/LC Study Group], Phys. Rept. **426**, 47 (2006) [arXiv:hep-ph/0410364], Sections 5.1 and 5.2.
- [12] K. Kawagoe, M. M. Nojiri and G. Polesello, “A new SUSY mass reconstruction method at the CERN LHC,” Phys. Rev. D **71**, 035008 (2005) [arXiv:hep-ph/0410160].
- [13] B. C. Allanach *et al.* [Beyond the Standard Model Working Group], arXiv:hep-ph/0402295; see the contribution by C. G. Lester, Section X.
- [14] C. G. Lester, M. A. Parker and M. J. White, “Determining SUSY model parameters and masses at the LHC using cross-sections, kinematic edges and other observables,” JHEP **0601**, 080 (2006) [arXiv:hep-ph/0508143].
- [15] N. Arkani-Hamed, G. L. Kane, J. Thaler and L. T. Wang, “Supersymmetry and the LHC inverse problem,” JHEP **0608**, 070 (2006) [arXiv:hep-ph/0512190].
- [16] J. M. Butterworth, J. R. Ellis and A. R. Raklev, “Reconstructing sparticle mass spectra using hadronic decays,” arXiv:hep-ph/0702150.
- [17] B. C. Allanach *et al.*, “The Snowmass points and slopes: Benchmarks for SUSY searches,” in *Proc. of the APS/DPF/DPB Summer Study on the Future of Particle Physics (Snowmass 2001)* ed. N. Graf, *In the Proceedings of APS / DPF / DPB Summer Study on the Future of Particle Physics (Snowmass 2001), Snowmass, Colorado, 30 Jun - 21 Jul 2001, pp P125* [arXiv:hep-ph/0202233].
- [18] D. J. Miller, P. Osland and A. R. Raklev, “Invariant mass distributions in cascade decays,” JHEP **0603**, 034 (2006) [arXiv:hep-ph/0510356].
- [19] We particularly thank Dirk Zerwas for several detailed discussions and emails.
- [20] T. Gleisberg, S. Hoche, F. Krauss, A. Schalicke, S. Schumann and J. C. Winter, JHEP **0402**, 056 (2004) [arXiv:hep-ph/0311263].
- [21] T. Sjostrand, S. Mrenna and P. Skands, JHEP **0605**, 026 (2006) [arXiv:hep-ph/0603175].
- [22] W. Porod, Comput. Phys. Commun. **153**, 275 (2003) [arXiv:hep-ph/0301101].
- [23] E. Richter-Was, D. Froidevaux and L. Poggioli, “ATLFAST 2.0: a fast simulation package for ATLAS”, Tech. Rep. ATL-PHYS-98-131 (1998); see also, H.T. Phillips, P. Clarke, E. Richter-Was, P. Sherwood, R. Steward [http://root.cern.ch/root/Atlfast.html].